Airborne eddy covariance measurements of ocean-air VOC fluxes: Distinguishing signal from noise

Xin Chen[1,2], Dylan B. Millet[1], Glenn M. Wolfe[3], Erin R. Delaria[3], M. Julian Deventer[1], Markus Müller[4,*], Arne Schiller[4,**], Kenneth Lee Thornhill[5,6], Armin Wisthaler[4,7]

[1] Department of Soil, Water, and Climate, University of Minnesota, Saint Paul, MN, USA
[2] Department of Civil and Environmental Engineering, Massachusetts Institute of Technology, Cambridge, MA, USA
[3] NASA Goddard Spaceflight Center, Greenbelt, MD, USA
[4] Institute for Ion Physics and Applied Physics, University of Innsbruck, Innsbruck, Austria
[5] NASA Langley Research Center, Hampton, Virginia, USA
[6] Analytical Mechanics Associates, Hampton, Virginia, USA
[7] Department of Chemistry, University of Oslo, Oslo, Norway

[*] Now at Ionicon Analytik GmbH, Innsbruck, Austria
[**] Now at Department of Breath Research, University of Innsbruck, Innsbruck, Austria

Correspondence: Dylan B. Millet (dbm@umn.edu); Xin Chen (chen3849@umn.edu)

Abstract

Ocean-atmosphere exchange plays an important but uncertain role for many volatile organic compounds (VOCs). Airborne eddy covariance (EC) enables direct flux quantification over large areas, but VOC applications have largely been performed over land. Here we combine the EC methodology with aircraft-based measurements from the North Atlantic Aerosol and Marine Ecosystem Study (NAAMES) and use the results to characterize air-sea VOC fluxes and to elucidate random and systematic drivers of error. Using perturbation experiments, we show that uncorrelated sensor noise (USN) causes flux biases by obscuring the sensor-wind time lag; such biases are avoided by imposing a time-lag constraint (e.g., from a higher-flux compound or time). We define the flux signal-to-noise ratio SNR_f and characterize its dependence on USN and sampling regime. Results show a transition from a USN-dominated regime to one where SNR_f is limited by turbulent stochasticity. The NAAMES VOC fluxes are noise-limited, whereas H_2O and sensible heat fluxes lie respectively in turbulence-limited and transitional regimes. We provide a methodology for determining sensor noise levels needed for robust flux detection: for the NAAMES subset examined here, a factor of 7-23 USN reduction would enable 75 % (rather than 17 %) of measured VOC fluxes to attain $SNR_f > 3$. The airborne NAAMES results reveal VOCs with universally upward (e.g., dimethyl sulfide), downward (e.g., acetone), bidirectional (e.g., acetaldehyde), and undetectable (e.g., monoterpenes) air-sea exchange, with controls including wind speed and planktonic activity. Findings highlight the importance of USN for VOC flux quantification by airborne EC and lay a foundation for expanded use of this technique.

1. Introduction

The ocean acts as a source and sink for a wide range of atmospheric volatile organic compounds (VOCs) including hydrocarbons, oxygenated VOCs, halocarbons, reduced-nitrogen compounds, and sulfur-containing gases (Carpenter et al., 2012). This air-sea exchange has important impacts on atmospheric oxidation, aerosol formation, and ozone chemistry in the marine atmospheric boundary layer (MBL) (Zheng et al., 2021; Novak and Bertram, 2020; Pound et al., 2020; Sanchez et al., 2018; Read et al., 2012; Donahue and Prinn, 1990). Net exchange is driven by a concentration gradient across the ocean-atmosphere interface (Seinfeld and Pandis, 2006; Liss and Slater, 1974), and therefore depends on the air- and water-side production, loss, and transport processes that determine the gas-phase and dissolved VOC concentrations (Davie-Martin et al., 2020; Beale et al., 2015; Beale et al., 2013; Li et al., 2003). The resulting fluxes are in general poorly constrained and a source of significant budget uncertainty for many VOCs.

Observational estimates of ocean-atmosphere VOC exchange have primarily relied on indirect approaches. These include:

• *MBL concentration-based methods*. Air-sea fluxes have been assessed by applying mass-balance considerations to observed MBL concentrations. For example, Singh et al. (2003b; 2003a) inferred oceanic fluxes of cyanides, aldehydes, methanol, and acetone over the Pacific by assuming steady state between VOC entrainment at the MBL top, within-MBL production/loss, and net ocean exchange. Other work has characterized ocean uptake of acetone and acetonitrile based on concentration differences between air masses with varying degrees of marine influence (de Gouw et al., 2003; Warneke and de Gouw, 2001) and calculated aromatic/sulfur compounds fluxes from nocturnal accumulation rates within the MBL (Rocco et al., 2021; Lawson et al., 2020; Marandino et al., 2007).

• *Enclosure methods.* Ocean emission and uptake fluxes have been extrapolated from chamber and mesocosm observations at the sea surface. For example, Sinha et al. (2007) deployed mesocosm enclosures with online proton transfer reaction-mass spectrometry to estimate marine fluxes of methanol, acetone, acetaldehyde, isoprene and dimethyl sulfide (DMS). More recently, Uning et al. (2021) quantified sea-to-air fluxes of isoprene and monoterpenes using a floating flux chamber and adsorbent cartridges with subsequent laboratory analysis.

• *Flux-gradient and eddy accumulation techniques*. These micrometeorological approaches derive air-sea fluxes from the vertical concentration gradient over the ocean surface (flux-gradient method) or by collecting updrafts and downdrafts into separate reservoirs prior to quantification (relaxed eddy accumulation, REA). For example, Tanimoto et al. (2014) used a floating buoy to measure vertical gradients of acetone and DMS and applied the flux-gradient approach to quantify the associated air-sea fluxes. REA has been widely employed to measure DMS fluxes (Hintsa et al., 2004; Zemmelink et al., 2002), and the technique has recently been adapted to a single-compartment configuration (Banerjee et al., 2024).

• *Air-sea concentration difference.* The two-film model introduced by Liss and Slater (1974) is routinely combined with measured or estimated air-side and water-side concentration fields to compute air-sea VOC fluxes. Example applications include acetone (Fischer et al., 2012), DMS (Bell et al., 2021), acetaldehyde (Millet et al., 2010), methanol (Bates et al., 2021), methyl ethyl ketone (Brewer et al., 2020), acetonitrile (Williams et al., 2004), aromatics (Wohl et al., 2023), methanethiol (Wohl et al., 2024), and isoprene (Hackenberg et al., 2017).

Compared to the traditional approaches above, eddy covariance (EC) enables more direct quantification of air-sea VOC fluxes with no physical disruption to the conditions driving exchange (Novak et al., 2022; Phillips et al., 2021; Vermeuel et al., 2020; Kim et al., 2017; Yang et al., 2014b; Yang et al., 2014a; Marandino et al., 2013; Yang et al., 2013; Marandino et al., 2009; Miller et al., 2009; Marandino et al.,

2008, 2007; Marandino et al., 2005). Fluxes are derived based on the turbulent correlation between tracer and vertical wind anomalies, and the technique requires high-frequency measurements that can resolve these correlations across the range of eddy scales. Airborne EC has shown particular potential for addressing VOC science questions (Pfannerstill et al., 2024; Yu et al., 2017; Wolfe et al., 2015; Yuan et al., 2015; Misztal et al., 2014; Karl et al., 2013). However, VOC applications over oceans have so far been limited to DMS (Conley et al., 2009; Faloona et al., 2005; Stevens et al., 2003; Bandy et al., 2002; Mitchell, 2001) and the MBL sulfur cycle (Novak et al., 2021).

In this work, we use the airborne EC framework to interpret VOC observations from the North Atlantic Aerosol and Marine Ecosystem Study (NAAMES). We explore the measurement and environmental factors controlling VOC flux detectability and flux errors in a marine context and interpret the resulting exchange in terms of present understanding and underlying drivers. Our work clarifies the viability and utility of airborne EC for characterizing ocean VOC fluxes and lays out requirements for more extensive application in the future.

2. NAAMES campaign and measurements

NAAMES (**Fig. 1 and S1**) was an NASA Earth Venture Suborbital (EVS) investigation combining ship-, aircraft-, and satellite-based observations to study marine phytoplankton activity and ocean-atmosphere interactions in the Western Subarctic Atlantic (39-56˚N, 46-37˚W) (Behrenfeld et al., 2019). This region hosts a large annual phytoplankton bloom that comprises a significant portion of global marine biological productivity (Behrenfeld and Boss, 2018; Behrenfeld, 2010). Four field campaigns were conducted during the main phases of the plankton annual cycle: NAAMES-1 (11-12/2015), NAAMES-2 (05-06/2016), NAAMES-3 (08-09/2017), and NAAMES-4 (03-04/2018). NAAAMES-1, 2, and 3 featured airborne measurements of trace gases, aerosols, and clouds onboard the NASA C-130 aircraft. The C-130 flights included multiple low-level MBL legs (detailed in Sect. 4.1), satisfying one of the prerequisites for deriving air-sea fluxes by airborne EC.

VOC mole fractions were measured on-board the C-130 by proton-transfer-reaction time-of-flight mass spectrometry (PTR-ToF-MS) during NAAMES-1 (for 4 of the 7 flights), NAAMES-2 (9 of 11 flights), and NAAMES-3 (9 of 12 flights). The employed instrument is an upgraded version of the prototype PTR-ToF-MS 4000 described by Müller et al. (2014) and manufactured by IONICON Analytic GmBH (Innsbruck, Austria). VOCs were sampled from outside the aircraft boundary layer using a winglet and a heated (50°C) ¼″ surface-treated stainless-steel line (Sulfinert®, Restek Corporation, Bellefonte, PA, USA). During NAAMES the winglet was positioned in a downward-facing orientation at the fuselage of the C-130. The inlet flow varied with ambient pressure from 15 standard liters per minute ($L \cdot min^{-1}$) at high altitudes to 30 $L \cdot min^{-1}$ at sea level. Reported analytes were calibrated via dynamic dilution of a certified compressed-gas standard (Apel-Riemer Environmental, Inc.), and sensitivities during NAAMES ranged from 320 $cps \cdot ppb^{-1}$ for methanol to 2206 $cps \cdot ppb^{-1}$ for methylethyl ketone. One-second concentration limits of detection were in the low 10s of ppt for most compounds, with an overall range of 9 ppt for toluene to 229 ppt for methanol. Zeroing was performed by passing ambient air through a Pt/Pd catalyst heated to 350°C (Müller et al., 2014). The instrument achieved a mass resolution ($m/\Delta m$, full-width half-maximum) of approximately 4000, with the mass axis calibrated through continuous addition of diiodobenzene (PerMassCal; IONICON Analytik GmbH, Innsbruck, Austria). The expected e-folding time (after accounting for inlet lag) for this instrument is approximately 0.1 s for most species targeted here but may be longer for sticky compounds (Müller et al., 2016). The NAAMES measurements were conducted at 5 Hz sampling frequency (selected as a compromise between response time, file size, and data load) with an estimated accuracy of 10 % + 5 ppt. **Table 1** lists the compounds examined in this study, which include methanol (detected as $CH_4O \cdot H^+$ at *m/z* 33.033), acetonitrile ($C_2H_3N \cdot H^+$, 42.034),

acetaldehyde ($C_2H_4O{\cdot}H^+$, 45.033), methanethiol ($CH_4S{\cdot}H^+$, 49.011), acetone ($C_3H_6O{\cdot}H^+$, 59.049), dimethyl sulfide ($C_2H_6S{\cdot}H^+$, 63.026), methylethyl ketone ($C_4H_8O{\cdot}H^+$, 73.065), dimethyl sulfoxide ($C_2H_6SO{\cdot}H^+$, 79.021), benzene ($C_6H_6{\cdot}H^+$, 79.054), toluene ($C_7H_8{\cdot}H^+$, 93.070), C8 aromatics ($C_8H_{10}{\cdot}H^+$, 107.086), C9 aromatics ($C_9H_{12}{\cdot}H^+$, 121.101), and monoterpenes ($C_{10}H_{16}{\cdot}H^+$, 137.132) (Pagonis et al., 2019). The mass used to measure isoprene ($C_5H_8{\cdot}H^+$, 69.070) was affected by contamination issues and we therefore omit this compound. The monoterpene signal was corrected for fragmentation to *m/z* 81.070 (~ 50 %) and 95.086 (minor); fragmentation to *m/z* 93.070 and 79.054 was insignificant due to the soft ionization conditions. Acetone and MEK are detected with their isomeric aldehydes (propanal; n-butanal + 2-methylpropanal). However, observations during the Atmospheric Tomography Mission (ATom) over the North Atlantic show the ketones to be dominant in this environment, with aldehyde:ketone ratios of 0.02-0.05 (propanal:acetone) and 0.16-0.23 (n-butanal:MEK; 2-methylpropanal was not detected) (Thompson et al., 2022; Apel et al., 2021; Wofsy et al., 2021). Furthermore, n-butanal is strongly fragmented (> 50 %) by the first-generation PTR-ToF-MS ion funnel deployed during NAAMES and was primarily detected at *m/z* 55.054 rather than 73.065. We therefore presume the NAAMES measurements of ∑(acetone + propanal) and ∑(MEK + n-butanal + 2-methylpropanal) to be dominated by acetone and MEK for the discussion that follows. The remaining masses above are assumed here to be dominated by the individual species listed.

Winds were measured onboard the C-130 using the NASA Langley Turbulent Air Motion Measurement System (TAMMS) at a frequency of 5 Hz (in 2016) and 20 Hz (in 2017). Like its previous iteration (Thornhill et al., 2003), the system uses fast-response flow-angle and temperature sensors to determine the wind with respect to the aircraft, and employs an Applanix 650 inertial navigation system (Applanix Inc.) to provide the aircraft's position, speed and attitude. Ambient air temperature measurements needed to determine true air speed are made with a Rosemount Model 102 non-deiced total air temperature sensor with a fast-response platinum sensing element (E102E4AL). Three-dimensional winds are computed from the full air motion equations (Lenschow, 1986) and corrected for aircraft motion as described by Thornhill et al. (2003) based on statistics derived from calibration maneuvers performed throughout the multi-year NAAMES EVS campaign. No additional corrections were required, and the uncertainty in the resulting wind fields is estimated at 10 %.

Other C-130 datasets employed in our analysis include flight navigation and housekeeping information (NASA/LARC/SD/ASDC, 2022, 2020), water vapor mole fractions (LI-7200, LI-COR Inc.), and potential temperatures.

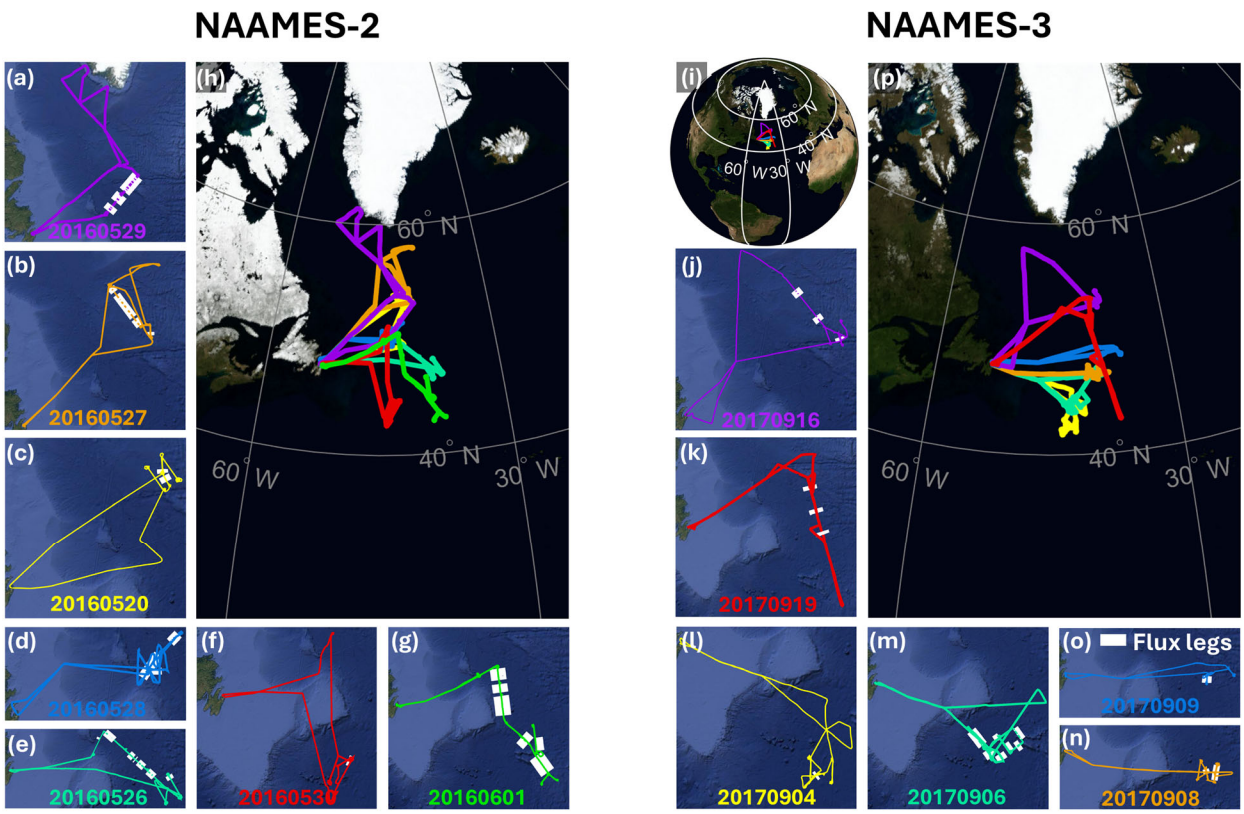

Figure 1. NAAMES flight tracks used to quantify air-sea fluxes. Panels (a-g) and (j-o) show the individual flights with flux legs indicated as white blocks (two legs in 20170906 vertically overlap in part and are not visually distinguishable). Panels (h) and (p) show the ensemble of flux-relevant flight tracks for each NAAMES phase colored by flight number (the full set of NAAMES flight tracks are shown in **Fig. S1**). Panel (i) shows the geographic location of the NAAMES study area. Basemaps are Blue Marble: Next Generation © 2004 NASA Earth Observatory (panels h, i, p) and GoogleSat © Google (all other panels).

3. Ocean-air VOC exchange indicated by MBL vertical gradients

Figure 2 shows median VOC profiles over the North Atlantic as measured during NAAMES-1, 2, and 3. The observed vertical structure differs between species and reflects distinct controlling processes including air-sea exchange. For example, DMS, DMSO, and CH_3SH concentrations are enhanced near the ocean surface, consistent with their known ocean source (Novak et al., 2022; Hoffmann et al., 2016). Monoterpenes and toluene also exhibit near-surface enhancements during NAAMES (Rocco et al., 2021; Yassaa et al., 2008). In contrast, acetone, methanol, and acetonitrile are depleted in the lowermost atmosphere, implying net ocean uptake during the sampling period. Cases with varying profile shapes across campaigns (acetaldehyde, MEK, C8/9 aromatics) or with little vertical gradient (benzene) could indicate weak, bidirectional, or seasonally varying exchange.

The concentration profiles are influenced to varying degrees by air-sea exchange, but they also incorporate effects from transport, atmospheric chemistry, and cloud processing. Separating these influences based on concentration measurements alone is not direct or straightforward. EC provides an avenue for direct surface-atmosphere flux quantification, and we proceed next to explore the application of this technique to the NAAMES airborne dataset.

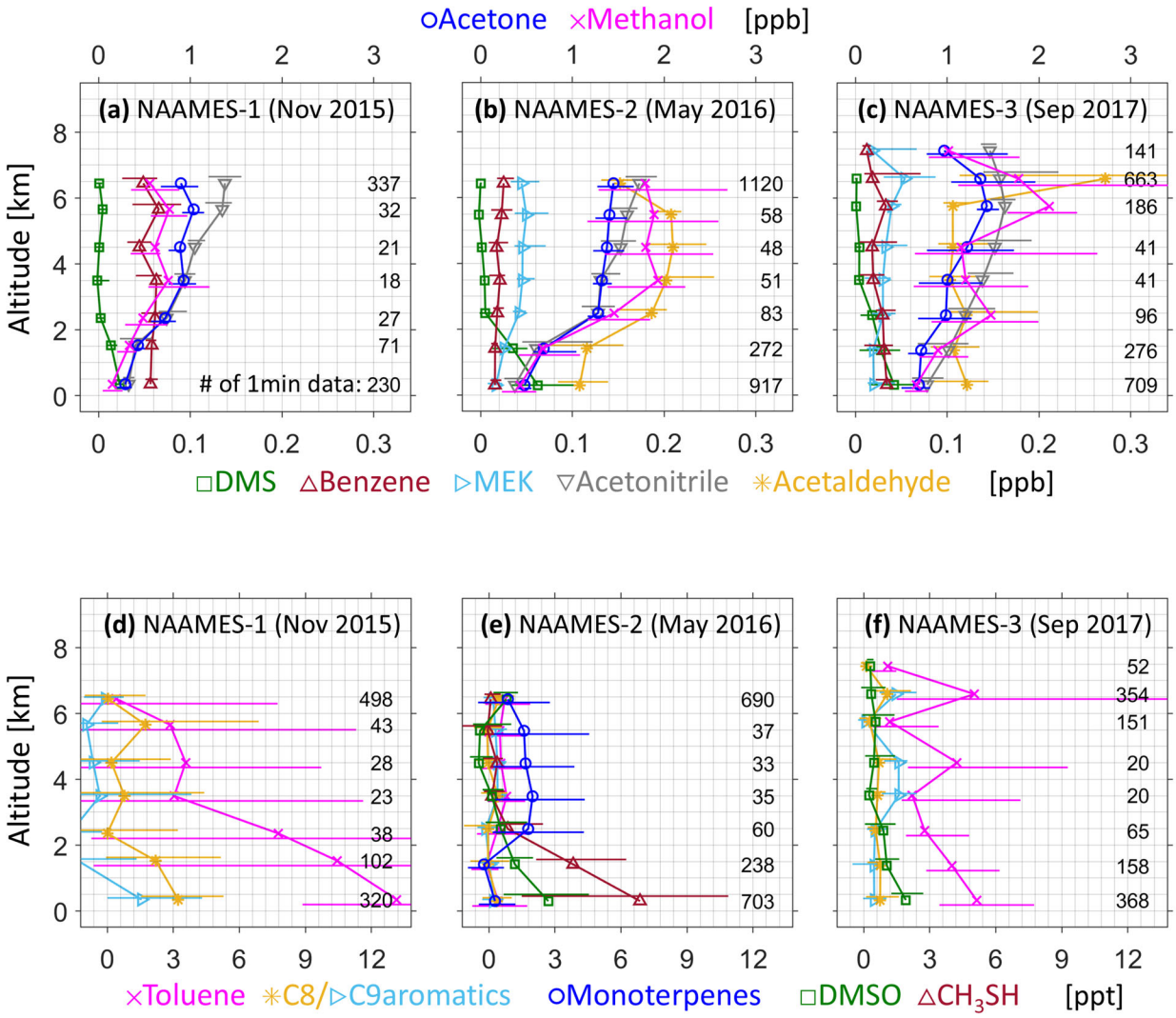

Figure 2. VOC vertical profiles observed during NAAMES-1, 2, and 3. Data plotted reflect the campaign-median concentrations (with interquartile range) in 1-km bins as measured over open ocean (east of 45 ˚W, 48 ˚W, and 46 ˚W for NAAMES-1, 2, and 3, respectively) along the flight tracks shown in **Fig. S1**. Right-aligned values indicate the mean number of valid 1-min data points across species in each vertical bin. Acetaldehyde and methanol data during flight 20151123 (NAAMES-1) are affected by isomeric interferences and are filtered accordingly. Flight 20160520 (NAAMES-2) is pollution-influenced and excluded here to better reflect the remote marine atmosphere. Instrument background subtraction imparts a systematic uncertainty of ±5 ppt to the values plotted above but does not affect the flux analyses.

4. Quantifying airborne eddy covariance fluxes and their uncertainties

4.1 Data pre-processing

Airborne EC analysis begins with steps for flux leg selection, signal detrending and filtering, and time-lag correction. We first temporally align the wind and VOC data on a common 5 Hz time base via nearest-neighbor matching (for the 5 Hz wind data in 2016) or bin-averaging (for the 20 Hz wind data in 2017). We next identify all prospective flux legs, defined as level (±34 m) flight intervals in the lower

atmosphere, with roll and pitch less than approximately 5°, that are ~3 min or more in duration (24 km at an average C-130 airspeed of 132 $m \cdot s^{-1}$) to ensure adequate sampling across eddy scales and a statistically robust number of data points. We also require that each leg has a quantifiable VOC-wind lag time as detailed later in this section. **Table S1** lists the 44 flux legs from 13 NAAMES-2 and NAAMES-3 flights identified in this way, which average 9 min (~72 km) in duration and range from 3-25 min (~20-210 km) at mean sampling altitudes of 126-219 m. Mean airspeeds range from 111-157 $m \cdot s^{-1}$ across the flux legs, corresponding to approximately one 5 Hz data point per 22-31 m.

The resulting data subsets undergo mean-removal and detrending to isolate the scalar concentration fluctuations that are driven by turbulence. We employ 100 s (11-16 km) moving-average mean removal; as shown in the **Supplementary Spectra** this acts as a high-pass filter to remove low-frequency, non-turbulent components (e.g., caused by air mass variability) that might not be excluded with a simple linear detrend (Novak et al., 2021; Moncrieff et al., 2005).

The time lags between scalar and wind measurements are next determined based on the maximum cross-covariance between the VOC concentration and vertical wind speed (w) within 0 ± 50 s, first applying a 0.02 Hz high-pass filter via Fast Fourier Transform (FFT) to remove any low-frequency covariance trends. This filter enables more accurate time-lag determination but is omitted from the subsequent variance partitioning, flux, and error calculations. In multiple cases the cross-covariance for an individual flux leg lacks a sufficiently clear peak for time-lag diagnosis (**Fig. 3**), and we therefore employ two alternative treatments as follows. (1) Flight-specific: here the time lag is defined based on the strongest cross-covariance peak for any species across the entire flight. The 13 lags calculated in this manner range from 0.4-10.8 s. (2) Species- and leg- specific: here the time lag is allowed to be species- and flight-leg specific. For both treatments, the derived lag times primarily reflect clock offsets between the PTR-ToF-MS and wind measurement systems, which varied by flight; the physical lag time expected for the 3.3 m (0.3175 cm ID) inlet with flows exceeding 15 $L \cdot min^{-1}$ is < 0.1 s.

Treatment 1 above assumes that the targeted VOCs interact similarly with the sampling inlet and instrument, and that inter-species lag differences mainly reflect statistical artifacts. Fluxes derived in this way are conservative relative to those obtained with treatment 2, which (in addition to clock synchronization) allows for species-specific sampling effects and tends to derive the largest possible flux magnitude. In the following analysis we use treatment 1 (a single flight-specific lag applied across species) as default.

4.2 Flux derivation

EC fluxes are computed from the pre-processed, high-resolution scalar and vertical wind time series obtained above. We employ both traditional and wavelet-based flux calculations to test the robustness of our results; the wavelet approach also provides temporally- (and for airborne fluxes, spatially-) resolved information within each flux leg.

Traditional ensemble-average EC calculations are performed strictly in the time domain, with fluxes calculated from the covariance between w and the scalar at hand (s, e.g. VOC mole fraction, water vapor mole fraction, or potential temperature) over a given analysis interval:

$$f = \overline{w's'}, \quad (1)$$

where primes reflect deviations from the mean and the overbar indicates time averaging. With the above units f takes the form of a kinematic flux (e.g., $ppb \cdot m \cdot s^{-1}$); scaling by the atmospheric number density then converts to an areal flux (e.g., $molec \cdot cm^{-2} \cdot s^{-1}$). Spectral information is subsequently obtained via FFT for quality assessment.

Wavelet transformation is an alternative approach that decomposes the s and w time series into both time and frequency space (Torrence and Compo, 1998) through application of a wavelet transfer function. This yields the corresponding wavelet coefficients (W_s, W_w), with the s-w cospectrum obtained as the real part of the cross-wavelet spectrum $W_s W_w^*$ divided by its corresponding scale (Liu et al., 2007). Integrating the cospectral power across frequency scales generates the time-resolved wavelet flux series, while averaging over time collapses all the local cospectral slices into a global cospectrum that can then be compared to the FFT cospectrum associated with traditional EC. In analyses here we include the cone of influence (Torrence and Compo, 1998) to prevent systematic underestimation relative to the traditional flux estimates (Wolfe et al., 2018). **Fig. S2** shows that the resulting wavelet-based flux estimates agree well with traditional EC results (R^2 values ≥ 0.95; zero-intercept slopes $\in [0.89, 1.07]$; values are within 30 % in 83 % of cases).

4.3 Spectral analyses

Spectral analysis provides frequency-resolved information to diagnose EC noise effects, assess high or low frequency flux attenuation, identify dominant flux-carrying eddy scales, and compare traditional versus wavelet-based results. The **Supplementary Spectra** file presents a full spectral analysis for the entire NAAMES airborne EC dataset, with example results shown in **Fig. 3**. The overall results indicate that: (1) the FFT spectra are in general agreement with the wavelet-based findings; (2) the VOC power spectra flatten out at higher frequencies, suggesting a white noise impact; and (3) the VOC-w cospectra are noisy but do not show any evidence of systematic high- or low-frequency flux loss.

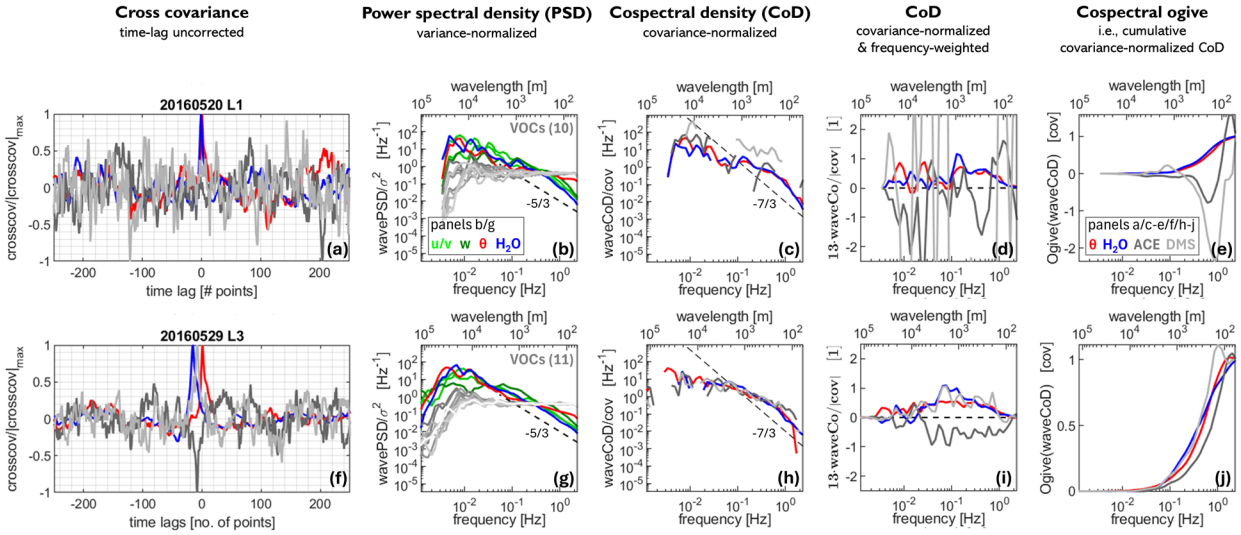

Figure 3. Example s-w cross-covariances (panels a, f) and wavelet-based spectral analyses (b-e, g-j). The top row shows an example flux leg in which clear cross-covariance peaks and well-behaved cospectra/ogives are obtained for water vapor (H_2O) and potential temperature (θ) but not for VOCs. The bottom row shows an example leg with clear cross-covariance peaks and reasonably well behaved cospectra/ogives for all plotted scalars. The impact of white noise on the VOC measurements is evident in the high-frequency range of the power spectra in panels (b) and (g). The wavelength scale is computed as the aircraft ground speed divided by frequency, without any height scaling. Line breaks in panel (c) occur where the flux power is in the opposite direction to that of the overall (net) flux value.

4.4 Flux error budget

In this section we examine potential error sources affecting the NAAMES flux analysis, with the aim of drawing broader conclusions that can inform future airborne VOC measurements. The following processes may contribute systematic and/or random errors to the computed fluxes:

A. *Sensor calibration errors*. A calibration bias for the VOC or vertical wind measurement would cause a systematic flux error of the same magnitude. We estimate these at 10 % each and 14 % combined (see **Sect. 2**).

B. *High-frequency attenuation*. Loss of high-frequency flux contributions can arise from an insufficient sampling frequency, inadequate instrument time response, or inlet-line damping. If uncorrected, the result is a systematic flux underestimate. The NAAMES VOC-w cospectra do not show systematic evidence of such an effect when compared to those for the non-VOC scalars (**Fig. 3**, **Supplementary Spectra**). Specifically, across all 44 flux windows we identify only one instance where there is any indication of high-frequency flux loss (flight 20170908 L2). It is possible that the instrument noise is obscuring attenuation in some of the other cases, but since there is no direct evidence of a systematic impact we perform no high-frequency correction and expect that other error sources are more important.

C. *Low-frequency losses*. A sampling duration that is too short to capture the largest-scale eddies will cause a systematic flux underestimate. The ogives (plateauing at low frequencies) and 95 % eddy scales (on average < 10 % of the leg length) seen during NAAMES indicate that such losses are unimportant for this study(**Fig. 3**, **Supplementary Spectra, Table S1**).

D. *Non-stationarity.* Variability contributed by larger-scale, non-turbulent motion can bias computed fluxes in a positive or negative direction. We do not view this as a predominant error source for NAAMES given the detrending approach used and given the agreement between traditional EC results and wavelet-based results (which do not require stationarity (Göckede et al., 2019)).

E. *Uncorrelated sensor noise (USN).* USN leads to random flux errors and can also cause systematic errors (e.g., via the time lag effects described next). Both aspects will be examined here.

F. *Time lag.* When USN is large relative to the flux-driven concentration fluctuations, estimates of the wind-scalar time lag (based on their cross-covariance) may be inaccurate (Langford et al., 2015). This leads to a systematic bias in the derived flux (**Sect. 4.6**) and is one way that random measurement uncertainties can cause systematic flux errors.

G. *Turbulent stochasticity.* The stochastic nature of turbulence can cause random flux errors due to incomplete statistical sampling across eddy scales. If USN and turbulent stochasticity are the predominant random error sources, the latter term can be estimated as the residual between the total flux random error and the USN-driven error:

$$\sigma_{f,RE}^2 = \sigma_{f,USN}^2 + \sigma_{f,turb}^2, \quad (2)$$

Here and throughout the remaining text, we denote variances related to fluxes with a subscripted f; those related to scalar quantities use a subscripted s (or w for vertical wind). Of the above errors, A and G are straightforward to assess while B-D are not expected to predominate for NAAMES. In the following sections we therefore focus on terms E and F and determine their impacts on the flux error budget by: 1) Quantifying the total flux random error and the flux random error caused by USN; and 2) Conducting noise perturbation experiments to characterize the random versus systematic impacts of USN and time-lag uncertainty on the computed fluxes. The same experiments then allow us to quantify the relative effects of USN and turbulent stochasticity on the flux signal-to-noise ratio.

4.5 Flux random error: quantification, partitioning, and impact on signal-to-noise ratio

We tested four empirical approaches for computing the total flux random error ($\sigma_{f,RE}$), based on: (i) the standard deviation of the scalar-wind covariance away from the true time lag (Spirig et al., 2005; Wienhold et al., 1995); (ii) a modified version of (i) that also accounts for cross-covariance offsets (Langford et al., 2015); (iii) the $\overline{w's'}$ standard error (Wolfe et al., 2015); and (iv) the variance of the scalar-wind covariance (Bendat and Piersol, 2010; Finkelstein and Sims, 2001). The results from these approaches agree closely (R > 0.82) across NAAMES VOCs, with approach (iii) giving generally lower error estimates. In what follows we report flux random errors based on the Spirig-Wienhold approach (i), which range from 0.006-7 ppt·m·s^{-1} (1σ; 0.02-27 μmol·m^{-2}·d^{-1}) for VOC cases in which the traditional versus wavelet fluxes agree to within 30 %. These random errors (**Fig. 4**) are insensitive to time lag uncertainties; as will be seen, the same is not true of the systematic error component.

The flux random errors arise from both USN and turbulent stochasticity (**Eq. 2**). To quantify the USN contribution ($\sigma_{f,USN}$), we first use autocovariance analysis (Lenschow et al., 2000) to partition the variability in scalar concentration (mean-removed and detrended) or in vertical wind to its USN versus atmospheric contributions (e.g., $\sigma_{s,tot}^2 = \sigma_{s,USN}^2 + \sigma_{s,turb}^2$). Any negative contributions derived in this way are set to zero with the sum conserved. **Fig. S3** shows that during NAAMES the VOC scalar variance is dominated by USN (98 % of $\frac{\sigma_{s,USN}^2}{\sigma_{s,tot}^2}$ ratios exceed 50 %), whereas turbulence dominates the observed scalar variance for H_2O, θ, and w—consistent with the power spectra behavior. We next construct an ensemble of Gaussian white noise realizations (a reasonable treatment based on the spectral analyses) with USN variance ($\sigma_{s,USN}^2$) prescribed according to the autocovariance results for each scalar. For each realization, we calculate the standard deviation of the cross-covariance between the resulting noise timeseries and w (away from the true time lag). As the scalar here is entirely noise, this standard deviation is equivalent to $\sigma_{f,USN}$ in **Eq. (2)**. Ten such realizations are averaged to obtain the final $\sigma_{f,USN}$ values for each scalar.

The empirical approach outlined above combines ideas from Lenschow et al. (2000), Langford et al. (2015), and Wolfe et al. (2015), and is referred to as LLW hereafter. When we compare the resulting $\sigma_{f,USN}$ estimates to the $\sigma_{f,RE}$ values obtained earlier we find that the total flux random error is dominated by the USN contribution for VOCs (92 % of $\frac{\sigma_{f,USN}^2}{\sigma_{f,RE}^2}$ ratios exceed 50 %, with smaller ratios for species with better-resolved fluxes) but by turbulent stochasticity for θ and H_2O. This flux-based finding aligns with the concentration-based autocovariance results above and shows that the VOC flux measurements are occurring in a noise-limited regime. The situation therefore differs from that encountered for air-sea flux measurements of CO_2, where sampling uncertainties are often the principal random error source (Dong et al., 2021).

We can next define a flux signal-to-noise ratio as $SNR_f = \frac{f}{\sigma_{f,RE}}$ (**Fig. 4**). SNR_f is analogous to the conventional concentration-based SNR definition: there, the signal is the measured concentration and the noise is the instrument precision, while here the signal is the measured flux and the noise is the total flux random error (due to USN and turbulent stochasticity). The flux limit of detection (LOD) can then be defined as the flux at which $SNR_f = 3$.

Analyses above showed for the VOCs measured during NAAMES that USN has a large impact on the total flux random errors; as a result, only 13 % of the derived fluxes have $SNR_f \geq 3$. The NAAMES VOC dataset thus presents a case where comparatively large USN contributes to low SNR_f and elevated flux

LODs. Below, we conduct noise perturbation experiments to quantify the systematic and random impacts of USN on the derived fluxes and on SNR_f, with a goal of clarifying sensor requirements for future airborne flux missions.

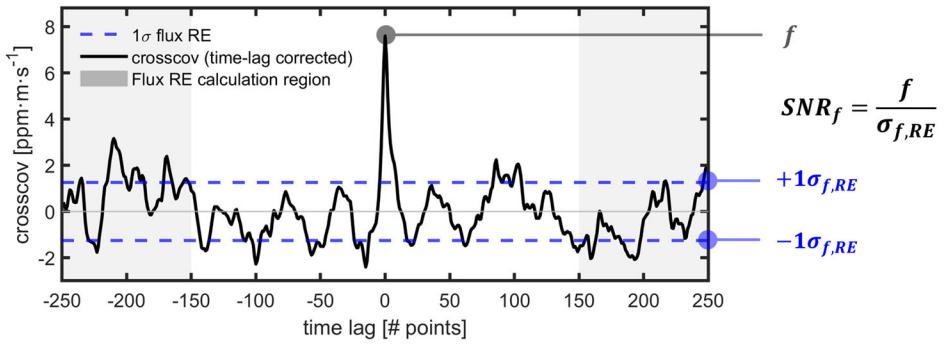

Figure 4. H_2O scalar-wind cross-covariance (crosscov) from NAAMES flight 20160520 L1, illustrating the flux signal-to-noise ratio (SNR_f). The flux random error ($\sigma_{f,RE}$) is estimated using the Spirig-Wienhold approach (Spirig et al., 2005; Wienhold et al., 1995). Figure format follows Langford et al. (2015).

4.6 Sensor noise causes systematic flux errors: Results from noise perturbation experiments

The H_2O concentration measurements from 11 NAAMES flux legs during 3 flights (20160528, 20160529, 20160601) exhibit well-behaved power spectra and we use them here as archetypical flux-driven signals without significant noise impacts. We impose Gaussian white noise ($\sigma^2_{imposed}$) onto these selected concentration signals at five different power levels according to $log_{10}\left(\frac{\overline{[H_2O]^2}}{\sigma^2_{imposed}}\right) =$ 4.5, 3.5, 2.5, 1.5, 0.5, with the levels selected such that results range from H_2O-like to VOC-like in the context of NAAMES. For a given signal and noise level, 500 random noise realizations are conducted (total: 27,500). These simulations are conducted separately for scenarios in which the scalar-wind time lag is (i) known and prescribed, and (ii) computed separately for each realization.

When the scalar-wind time lag is known and prescribed, the 500 fluxes derived in this way at a given noise level approximate a normal distribution centered approximately on the true value—with increasing spread at higher noise (**Fig. 5**). Conversely, when the time lag is computed separately for each realization, the 500-flux ensemble is no longer centered on the true value for the higher noise scenarios. Rather, a ghost peak appears—with a subset of the ensemble exhibiting spurious fluxes in the opposite direction of around the same magnitude. Eventually, both mirrored populations exceed the true flux magnitude, as random spikes in the noise-wind cross-covariance exceed the actual H_2O-wind covariance. In such cases, the true flux is obscured by the noisy cross-covariance, and searching for the maximum on a case-by-case basis tends to overestimate the flux magnitude with random direction. The phenomenon parallels the mirroring described by Langford et al. (2015). In the high-noise limit, we see from **Fig. 5** that the average over an ensemble of measurements converges to approximately the true flux in the prescribed time-lag scenario, but it converges to near-zero in the non-prescribed scenario. In this way, random errors in the form of USN can yield systematic flux errors by inhibiting accurate determination of the scalar-wind time lag. For situations where a significant number of the fluxes are near or below the LOD, time lags should when possible be prescribed (e.g., from proximate higher-flux periods, or based on higher-flux co-measured compounds) to avoid imposing a systematic bias on the results.

For the duration of the noise perturbation analysis here we proceed with the prescribed time-lag results. For each realization, the spread across the 500-member flux ensemble then characterizes the uncertainty associated with the contaminated H_2O flux that is due to the imposed random noise: i.e., it estimates the same $\sigma_{f,USN}$ quantity that was derived earlier via LLW.

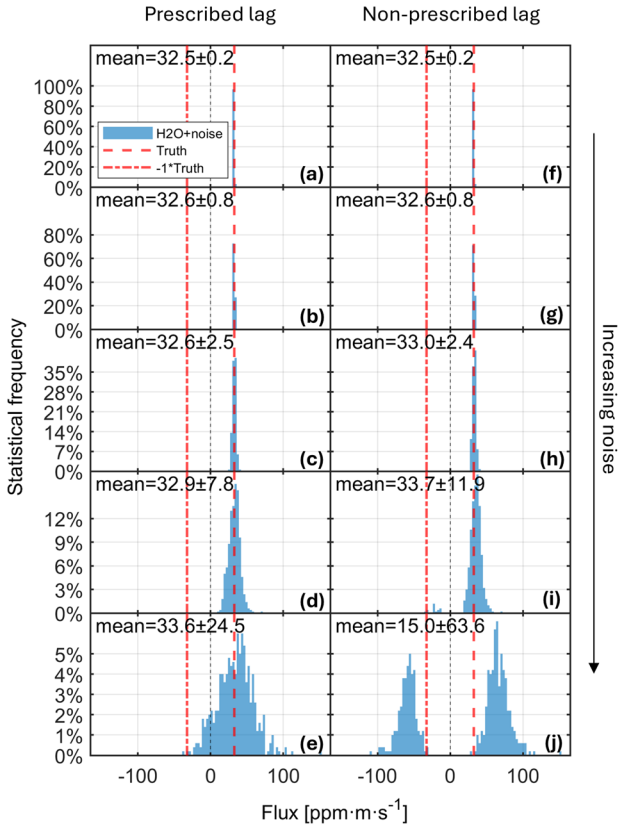

Figure 5. Flux histograms for the noise perturbation ensemble. H_2O fluxes from NAAMES flight 20160601 L1 are subjected to five different noise levels ($\sigma^2_{imposed}$) according to $log_{10}\left(\frac{\overline{[H_2O]^2}}{\sigma^2_{imposed}}\right) = 4.5, 3.5, 2.5, 1.5, 0.5$. Results are shown for scenarios in which the scalar-wind time lag is known (-2.2 s) and prescribed (a-e) and in which the time lag is determined independently (0 ± 10 s search window) for each flux derivation (f-j).

4.7 Sensor noise impacts on random flux errors

The results from the noise perturbation experiments allow us to empirically assess the propagation of scalar-based errors to flux-based errors that has been theoretically derived and applied in previous studies (Deventer et al., 2019; Wolfe et al., 2018; Langford et al., 2015; Peltola et al., 2014; Neftel et al., 2007):

$$\sigma_{f,USN} = \frac{\sigma_w}{\sqrt{N}}\sigma_{s,USN}, \quad (3)$$

Here, σ_w is the standard deviation of the vertical wind speed and N is the number of data points. **Equation (3)** takes a reduced form for NAAMES since USN for the wind measurement is negligible relative to that for the other scalars examined (Rannik et al., 2016; Peltola et al., 2014).

Plotting $\sigma_{f,USN}$ as a function of $\sigma_{s,USN}$ for the noise perturbation ensemble (**Fig. 6**) suggests a power law relation $y = Ax^K$. A linear regression between $\log_{10}\sigma_{f,USN}$ and $\log_{10}\sigma_{s,USN}$ for each flux leg reveals a consistent $K \sim 1$ (**Fig. S4a**), indicating a simple linear correlation $y = Bx$ throughout the data range. The resulting slope B is within 4 % of $\frac{\sigma_w}{\sqrt{N}}$ (**Fig. S4b**), with the NAAMES θ observations following the same leg-specific linear correlations as the contaminated and native H_2O data (**Fig. 6**). The regressions thus empirically validate the linearity and coefficients embedded in **Eq. (3)**.

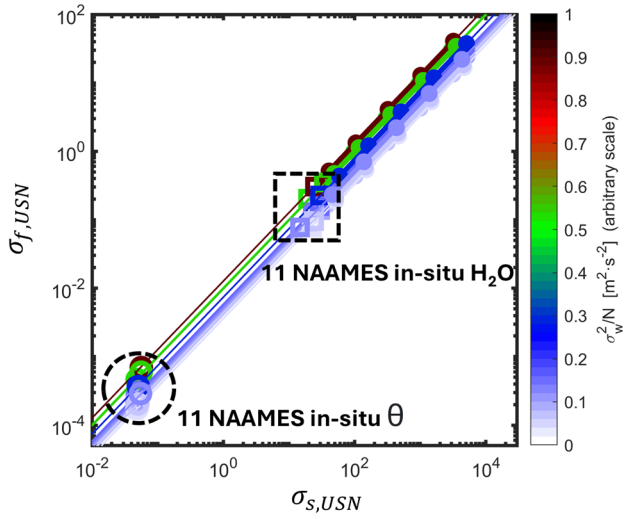

Figure 6. Impact of uncorrelated sensor noise on flux random errors. Results are shown for the noise perturbation ensemble described in-text (filled circles), for the uncontaminated NAAMES H_2O observations (squares), and for the NAAMES θ observations (hollow circles). Each plotted value for the noise perturbation ensemble reflects the mean across all 500 members (standard deviations are smaller than the data points and thus not visible). See **Fig. S4** for regression statistics.

4.8 Flux signal-to-noise ratio: impact of noise versus turbulence

Substituting **Eq. (3)** into **Eq. (2)**, normalizing by f^2, and rearranging, we obtain:

$$SNR_f = \left(\frac{\sigma_w^2}{Nx^2} + \frac{\sigma_{f,turb}^2}{f^2}\right)^{-0.5}, \quad (4)$$

where $x = \frac{|f|}{\sigma_{s,USN}}$ is used as an independent variable such that: (i) all scalars employ the same scale, and (ii) each 500-member ensemble is normally distributed in x and can be represented through its mean ± standard deviation. σ_w^2 and N are leg-specific quantities reflecting the turbulent regime and the sampling duration, respectively. $\sigma_{f,turb}$ is computed as a residual via **Eq. (2)**. The $\frac{\sigma_{f,turb}}{f}$ ratio quantifies the flux (relative) random error arising from turbulent stochasticity, and is affected by factors including boundary layer depth, measurement height, and sampling duration (Wolfe et al., 2018; Lenschow et al., 1994). Thus, for a given meteorological regime and sampling plan, it is mainly $x = \frac{|f|}{\sigma_{s,USN}}$ that differentiates the SNR_f behavior of different scalars.

Figure 7a plots SNR_f as a function of x (**Fig. S5** shows the same data on a log-log scale). Each curve shows the SNR_f:x dependence for a given flux leg with its associated duration and turbulent

characteristics. The impact of USN decreases from left to right so that the derivation of SNR_f in **Eq. (4)** is dominated by $\frac{\sigma_w^2}{Nx^2} = \frac{\sigma_w^2 \sigma_{s,USN}^2}{Nf^2}$ to the left (noise-limited regime) and by $\frac{\sigma_{f,turb}^2}{f^2}$ to the right (turbulence-limited). The spread between curves reflects the differing meteorology, sampling conditions, and flux magnitudes across legs.

The original H_2O flux observations (hollow squares) fall on the right-hand side of the corresponding leg-specific curves. The contaminated datapoints then define the transition, under those sampling conditions, to a noise-dominated regime. The in-situ θ (hollow circles) and VOC (triangles) fluxes for the same set of flux legs fall within the overall envelope delineated by the noise-contaminated H_2O data. This confluence demonstrates the broader representativeness of the plotted function curves: they define an SNR space that all scalars measured under similar sampling conditions should fall within.

Langford et al. (2015) defined an analogous SNR ($\frac{\sigma_{s,turb}^2}{\sigma_{s,USN}^2}$) for scalar concentration variance ($\sigma_{s,tot}^2$) that is related to the figure of merit Q ($\frac{\sigma_{s,USN}}{\sigma_{s,turb}}$) proposed earlier by Lenschow and Kristensen (1985a, 1985b). **Fig. 7(b)** plots the square root of Langford SNR as a function of x for the same set of data as shown in panel **7(a)**. Together, **Fig. 7(a-b)** thus conveys an overall transition in air-sea flux measurements with varying $x = \frac{|f|}{\sigma_{s,USN}}$. To the left is the noise-limited regime, where USN dominates $\sigma_{s,tot}$, and SNR_f is likewise controlled by USN in a manner that is modulated by turbulence and sampling. To the right, $\sigma_{s,tot}$ is turbulence-driven, and SNR_f approaches a maximum value that is limited by the randomness of that turbulence. The NAAMES H_2O fluxes are well within the turbulence-limited regime, while the θ fluxes fall mostly in the turbulence-limited regime and partly in the transition regime. The majority of the in-situ VOC measurements exhibit behavior resembling that of severely noise-contaminated H_2O data and fall within the noise-limited regime.

The results in **Fig. 7** provide a framework that can be used to assess whether an instrument's noise performance is sufficient for a given flux application and desired SNR_f. That is, for an expected flux magnitude, the plotted curves can be used to identify the maximum $\sigma_{s,USN}$ that is likely to yield an appropriate SNR_f under the NAAMES sampling conditions. For the 11 actual flux legs examined in **Fig. 7**, 17 % of the VOC fluxes have $SNR_f > 3$; for example, the mean (± SD) SNR_f value for acetone is 3.35±1.77 but just 0.53±0.51 for monoterpenes. We find that if USN was lowered by a factor of 7-23, 75 % of these VOC fluxes would exceed SNR_f=3. A 10-20× advance in instrumental noise performance compared to the PTR-ToF-MS deployed during NAAMES would therefore provide significant benefits in our ability to quantify ocean-air VOC fluxes.

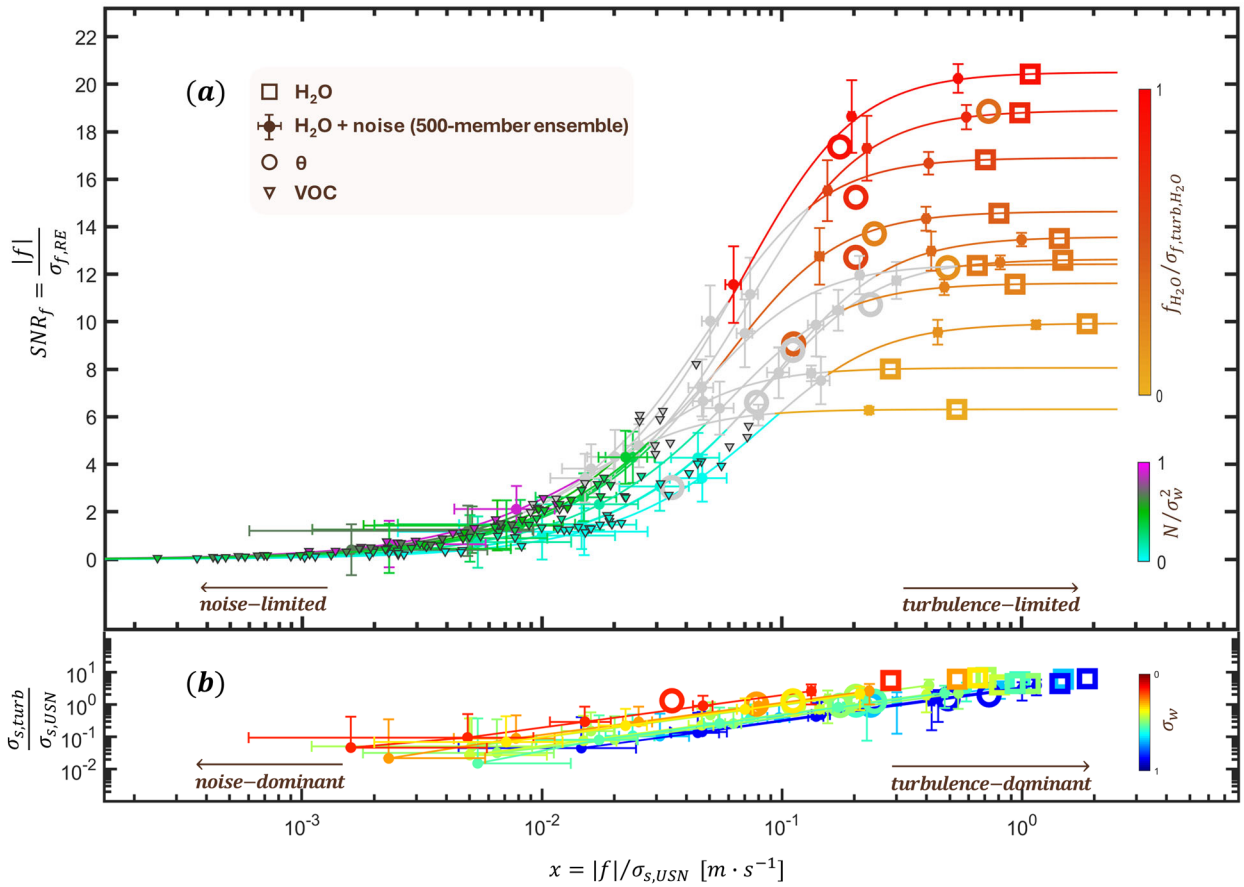

Figure 7. (a) Flux SNR (SNR_f) as a function of the flux:USN ratio. The curves visualize the $SNR_f - x$ relationship based on **Eq. (4)** for the 11 analyzed flux legs, and are colored (arbitrary scale) to indicate noise-limited (bottom colorbar), transitional (grey), and turbulence-limited (top colorbar) regimes. Datapoints indicate the noise perturbation ensemble (filled circles; 500-member mean and standard deviation) along with the NAAMES H_2O (hollow squares), θ (hollow circles), and VOC (triangles) observations. (b) Ratio of the turbulent- to USN-driven scalar concentration variability ($\frac{\sigma_{s,turb}}{\sigma_{s,USN}}$) as a function of the flux:USN ratio. Plotting conventions follow those of panel (a), with the noise perturbation ensemble represented by the 500-member median and interquartile range, and colors indicating the standard deviation of the vertical wind speed. $\sigma_{s,USN}$ and $\sigma_{s,turb}$ are derived from the variance partitioning analysis described in-text with negative values set to zero. Zero and negative values are omitted from the logarithmic scales. All fluxes employ traditional EC estimates with flight-specific lag times. Color bars use arbitrary scales.

5. NAAMES airborne VOC fluxes

We proceed to examine the VOC fluxes quantified during NAAMES, employing the flight-specific lag times as best estimates based on the results in **Sect. 4.6**. **Table 1** lists the mean flux, LOD, and number of above-LOD flux detections for each VOC during NAAMES. Flux legs that pass the selection criteria outlined earlier all occur during NAAMES-2 (May/June 2016) and NAAMES-3 (September 2017).

Across VOCs, acetone and DMS have the greatest number of flux measurements with magnitudes exceeding the corresponding observation-specific LOD (**Table 1**). The fraction of above-detection fluxes

for other species ranges from 0-21 %. However, analyses above showed that the NAAMES VOC flux errors and LODs are dominated by random USN effects, and it follows that these uncertainties are reduced through averaging. Accordingly, we see in **Table 1** that in some cases the magnitude of the campaign-mean flux (and/or the error-weighted mean flux) exceeds its uncertainty level—even with just a few above-detection flux measurements. These compound-specific results are discussed further in the next sections. In all cases the limited number of flux observations and the regional sampling during NAAMES mean that results need to be interpreted with caution in terms of their broader spatial/temporal representativeness.

Table 1. Summary of airborne VOC flux measurements during NAAMES.

VOC	Ion formula	*m/z*	Number of flux legs[a]	Flux range[a]	Campaign mean flux[a]	Uncertainty of the mean flux[b]	Error-weighted campaign mean flux[c]	Uncertainty of the weighted mean flux[d]	Above-LOD flux observations[e]
				($\mu mol \cdot m^{-2} \cdot d^{-1}$)					upward(↑) / downward(↓)
Acetone	$C_3H_6O \cdot H^+$	59.049	*40*	[−25.5, +3.7]	*−5.0*	*1.2*	−3.0	*0.45*	0↑ / 23↓
Dimethyl sulfide (DMS)	$C_2H_6S \cdot H^+$	63.026	*39*	[−1.3, +5.0]	+1.3	*0.52*	+0.61	*0.15*	12↑ / 0↓
Methanol	$CH_4O \cdot H^+$	33.033	*37*	[−38.1, +85.4]	+0.21	*3.8*	−2.9	*1.5*	1↑ / 5↓
Methylethyl ketone (MEK)	$C_4H_8O \cdot H^+$	73.065	*39*	[−2.1, +11.4]	+0.58	*0.35*	+0.093	*0.14*	6↑ / 2↓
Acetaldehyde	$C_2H_4O \cdot H^+$	45.033	*36*	[−5.8, +33.4]	+2.8	*1.4*	+0.45	*0.57*	4↑ / 2↓
Acetonitrile	$C_2H_3N \cdot H^+$	42.034	*34*	[−2.9, +3.5]	+0.18	*0.49*	+0.034	*0.18*	1↑ / 1↓
Benzene	$C_6H_6 \cdot H^+$	79.054	*31*	[−0.7, +2.0]	+0.34	*0.28*	+0.19	*0.13*	2↑ / 0↓
Methanethiol	$CH_4S \cdot H^+$	49.011	*16*	[−0.3, +1.4]	+0.21	*0.31*	+0.13	*0.11*	0↑ / 0↓
Dimethyl sulfoxide (DMSO)	$C_2H_6SO \cdot H^+$	79.021	*33*	[−0.8, +0.6]	+0.0089	*0.098*	+0.00050	*0.033*	0↑ / 0↓
Toluene	$C_7H_8 \cdot H^+$	93.070	*36*	[−0.9, +0.6]	+0.0058	*0.14*	+0.069	*0.070*	0↑ / 0↓
Monoterpenes	$C_{10}H_{16} \cdot H^+$	137.132	*17*	[−0.8, +1.1]	−0.015	*0.30*	+0.013	*0.15*	0↑ / 0↓
C8 aromatics	$C_8H_{10} \cdot H^+$	107.086	*19*	[−0.5, +0.4]	+0.0097	*0.15*	+0.023	*0.068*	0↑ / 0↓
C9 aromatics	$C_9H_{12} \cdot H^+$	121.101	*15*	[−0.1, +0.4]	+0.094	*0.11*	+0.046	*0.070*	0↑ / 0↓

[a,c]The traditional versus wavelet fluxes agree to within 30 %, including below-LOD fluxes.

[b,d]3σ uncertainty.

[b]Calculated via error propagation (Taylor, 1997; see Ch. 3).

[c,d]Computed following Taylor (1997; see Ch. 7).

[e]Number of flux measurements that exceed the corresponding observation-specific flux LOD (3σ).

5.1 Acetone deposition and DMS emissions: Wind and biological controls

The measured acetone and DMS fluxes are plotted by leg in **Fig. 8**. For acetone, detectable fluxes are all downward and the campaign-mean exchange rate is -5.0 $\mu mol \cdot m^{-2} \cdot d^{-1}$ [propagated 3σ uncertainty: ±1.2 $\mu mol \cdot m^{-2} \cdot d^{-1}$]. The corresponding error-weighted mean flux is -3.0 [±0.45] $\mu mol \cdot m^{-2} \cdot d^{-1}$. These values are comparable to prior shipborne EC results from the North Atlantic high latitudes (-4.8 to -11 $\mu mol \cdot m^{-2} \cdot d^{-1}$ from 40-65˚N) (Yang et al., 2014b; Yang et al., 2014a). However, the global ocean acetone flux is heterogeneous (Wang et al., 2020) and a net source has been reported over the subtropical and southern Atlantic (Yang et al., 2014b; Taddei et al., 2009).

Ocean-atmosphere VOC fluxes are driven both by the air-sea mixed layer concentration difference and by the associated exchange velocity (Liss and Slater, 1974), and the airborne acetone fluxes from NAAMES reveal the influence of wind speed on this exchange. Specifically, during both NAAMES-2 and NAAMES-3 the strongest acetone fluxes occurred when horizontal wind speeds were highest (flight 20160530: ~24 $m \cdot s^{-1}$; 20170919: ~12 $m \cdot s^{-1}$). **Fig. 8** shows that the largest September fluxes for DMS likewise occurred during flight 20170919. This is consistent with the NAAMES-3 cruise results, where wind was found to be the main driver of DMS flux variability (Bell et al., 2021).

All of the airborne DMS fluxes measured during NAAMES that exceed the LOD are upward, out of the ocean. The campaign-mean flux of +1.3 [±0.52] (error-weighted mean: +0.61 [±0.15]) $\mu mol \cdot m^{-2} \cdot d^{-1}$ matches ship-based EC results in the North Atlantic (40-65˚N) from the HiWinGS mission during fall 2013 (mean: +1.5 $\mu mol \cdot m^{-2} \cdot d^{-1}$) (Kim et al., 2017). DMS emissions estimated from the seawater concentrations measured during NAAMES-2 and NAAMES-3 ranged from +0.1 to +48 $\mu mol \cdot m^{-2} \cdot d^{-1}$, with a mean of ~7 $\mu mol \cdot m^{-2} \cdot d^{-1}$ (Bell et al., 2021). Surface EC measurements from the North Atlantic during other seasons (+2.7 to +18.1 $\mu mol \cdot m^{-2} \cdot d^{-1}$) (Land et al., 2014; Miller et al., 2009; Marandino et al., 2008) have also tended to be higher than the NAAMES airborne results.

The NAAMES airborne DMS fluxes are generally higher and more variable in spring 2016 (NAAMES-2) than in fall 2017 (NAAMES-3; **Fig. 8**), and this pattern aligns with the distinct biological regimes at these times (Behrenfeld, 2010). NAAMES-2 occurred during the phytoplankton climax phase with a median chlorophyll-a concentration in the study area of 1.3 $mg \cdot m^{-3}$ (interquartile range: 0.7-2.2 $mg \cdot m^{-3}$) and highly variable dissolved DMS concentrations (mean ± standard deviation: 3.9±2.7 nM) (Bell et al., 2021). NAAMES-3 occurred during the phytoplankton depletion phase when chlorophyll-a concentrations were far lower (0.3 [0.2-0.8] $mg \cdot m^{-3}$) and dissolved DMS concentrations were more uniform (3.1±1.0 nM) (Bell et al., 2021). The greater dissolved DMS variability during NAAMES-2 has been attributed to the combined effects of elevated biological activity and wind-driven dilution of sea-surface concentrations (Bell et al., 2021). The strong horizontal winds during NAAMES-2 thus affected the air-sea DMS fluxes both directly (via more efficient air-sea exchange) and indirectly (via dilution of the dissolved concentrations).

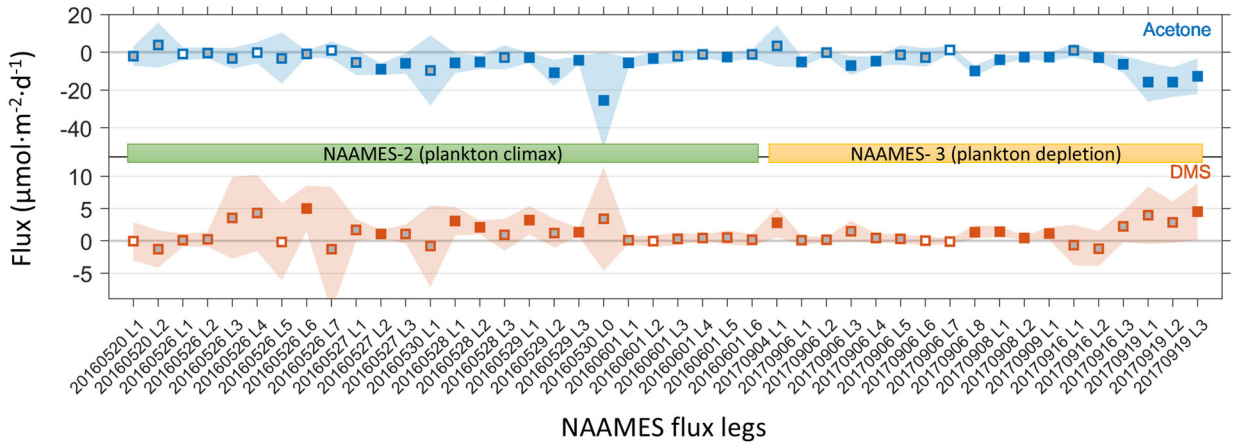

Figure 8. Airborne fluxes of acetone and DMS measured during NAAMES. Solid squares show EC-based estimates that i) agree with the wavelet-based results to within 30 % and ii) are above the corresponding LOD. White-filled squares indicate values where condition i) is not met; grey-filled squares indicate values where i) is met but ii) is not met.

5.2 Other VOCs

Of the remaining VOCs, acetaldehyde and MEK exhibit the clearest signatures of air-sea exchange, with 17% and 21 % of individual flux measurements falling above the associated detection limit (**Table 1**).

• *Acetaldehyde.* Bidirectional air-sea exchange of acetaldehyde has been reported for this region based on shipborne EC during the Fall 2012 AMT-22 mission (mean: 0.8 $\mu mol \cdot m^{-2} \cdot d^{-1}$) (Yang et al., 2014b). The NAAMES airborne results likewise indicate bidirectional exchange, with 4 upward and 2 downward above-LOD fluxes. The campaign-mean flux of +2.8 [±1.4] (error-weighted mean: +0.45 [±0.57])

549 μmol·m^{-2}·d^{-1} from NAAMES also falls within the spring/fall range for the subarctic Atlantic that has been
550 predicted by global models (0-7 μmol·m^{-2}·d^{-1}) (Wang et al., 2019; Millet et al., 2010).
551 • *MEK.* Prior vertical surveys over the tropical Pacific and in the remote southern hemisphere revealed
552 enhanced MEK near the ocean surface, suggesting an oceanic source (Brewer et al., 2020). Air-sea
553 exchange modeling for the Southern Ocean implies a net emission of ~0.1 μmol·m^{-2}·d^{-1} based on a
554 dissolved concentration of 0.88 nM (Brewer et al., 2020; Schlundt et al., 2017). The NAAMES airborne
555 fluxes over the Subarctic Atlantic are predominantly upward (6 upward and 2 downward above-LOD
556 values), and the campaign-mean oceanic emission of +0.58 [±0.35] (error-weighted mean: +0.093
557 [±0.14]) μmol·m^{-2}·d^{-1} is on the same order as the Brewer et al. (2020) estimates.

558 Methanol, acetonitrile, and benzene feature 2-6 individually-detectable fluxes, while individual flux
559 observations for the remaining VOCs all fall below the corresponding single-measurement LOD values.
560 Nevertheless, by averaging results we can reduce uncertainties in the mean measured fluxes and draw
561 comparisons to prior studies.
562 • *Methanol.* Methanol has one detectable upward flux under high wind speeds (+85.4 μmol·m^{-2}·d^{-1} on
563 flight 20160530) and five downward detectable fluxes (-7.2, -9.0, -9.5, -11.4, and -38.1 μmol·m^{-2}·d^{-1}).
564 The campaign-mean exchange rate of +0.21[±3.8] μmol·m^{-2}·d^{-1} and error-weighted mean of -2.9[±1.5]
565 μmol·m^{-2}·d^{-1} are both smaller than the deposition fluxes detected by shipborne EC over the Northeast
566 Atlantic (AMT-22 mean: -15 μmol·m^{-2}·d^{-1}, Fall 2012) and the Subarctic Atlantic (HiWinGS mean: -12.3
567 μmol·m^{-2}·d^{-1}, Fall 2013) (Yang et al., 2014b; Yang et al., 2014a; Yang et al., 2013). The mean of the five
568 downward detectable fluxes measured during NAAMES (-15 μmol·m^{-2}·d^{-1}), however, is very similar to
569 those prior shipborne EC results.
570 • *Methanethiol.* Based on monthly seawater concentrations extrapolated from field observations, Wohl et
571 al. (2024) calculated CH_3SH emission fluxes for the subarctic Atlantic that generally exceeded 1-3
572 μmol·m^{-2}·d^{-1}. The NAAMES flux is approximately an order of magnitude lower than that, averaging
573 +0.21 [±0.31] μmol·m^{-2}·d^{-1} (error-weighted mean: 0.13 [±0.11] μmol·m^{-2}·d^{-1}). Nevertheless, the
574 campaign-mean DMS:methanethiol flux ratio of 4-5 is in-line with prior EC-based (5.5) (Novak et al.,
575 2022) and calculated values (3.2-6.1) (Lawson et al., 2020; Kiene et al., 2017; Kettle et al., 2001).
576 • *Benzene/Toluene/C8 aromatics.* From measured seawater concentrations in the Southern Ocean and
577 Arctic, Wohl et al. (2023) inferred sea-to-air benzene and toluene emission rates of approximately +0.03
578 μmol·m^{-2}·d^{-1}. Meanwhile, mesocosm studies in the Southwest Pacific Ocean suggested benzene, toluene,
579 and C8 aromatic fluxes of +1.1, +0.9, and +0.8 μmol·m^{-2}·d^{-1}, respectively (Rocco et al., 2021). The mean
580 and error-weighted mean fluxes from NAAMES (including their uncertainty ranges) are significantly
581 lower than the mesocosm results and are closer to the Wohl et al. (2023) estimates (**Table 1**).
582 • *Acetonitrile.* Overall, it seems clear that the ocean acts as a net sink for acetonitrile as its concentrations
583 are usually depleted in the MBL (de Gouw et al., 2003; Li et al., 2003; Singh et al., 2003b). Singh et al.
584 (2003b) inferred an oceanic deposition flux of 0.2 μmol·m^{-2}·d^{-1} based on observations over the Pacific
585 ocean, but other work has shown that the marine CH_3CN sink varies strongly with location (de Gouw et
586 al., 2003). The airborne observations during NAAMES provide some indication of bidirectional
587 exchange (with 1 upward and 1 downward above-LOD fluxes), but the campaign-mean and error-
588 weighted mean exchange rates are statistically indistinguishable from zero—with uncertainties that
589 encompass the Singh et al. (2003b) estimate (**Table 1**).
590 • *Monoterpenes*. Prior shipborne EC measurements in the North Atlantic revealed bidirectional fluxes for
591 monoterpenes (averaging +0.04 μmol·m^{-2}·d^{-1}) (Kim et al., 2017). No detectable monoterpene fluxes were
592 measured and the campaign-mean exchange rate is likewise not distinguishable from zero (**Table 1**).
593 • *DMSO/C9 aromatics.* To our knowledge there have not been any reported air-sea exchange rates for
594 these species. Their fluxes were undetectable during NAAMES, and the uncertainty range for the

campaign-mean results suggests that any air-sea exchange that did occur had a magnitude less than approximately 0.1 $\mu mol \cdot m^{-2} \cdot d^{-1}$ (**Table 1**). However, it is possible that wall interactions may have inhibited flux detectability for these lower-volatility species.

5.3 Potential impact of flux divergence

Prior studies have examined the role of vertical flux divergence for VOCs in the MBL, focusing on DMS (e.g., Bandy et al., 2002; Stevens et al., 2003; Faloona et al., 2005; Conley et al., 2009) and its oxidation products (Novak et al., 2021). Processes that can lead to a change in EC-measured fluxes with height include: i) photochemical oxidation or production of a given VOC; ii) entrainment of VOC-depleted or VOC-enriched air from aloft; iii) horizontal advection / changing source footprint with height; or iv) cloud processing. The sign of the expected effect varies depending on the dominant process and on the source-sink profile for a given VOC. Flux legs analyzed here range in elevation from 126-219 m, and based on the gradients reported in the above-cited studies we expect air-sea exchange to be the predominant influence within that range. However, NAAMES did not include sufficient multi-level sampling for us to quantify the impact of vertical flux divergence across the study, and we cannot rule out its role entirely.

6. Remarks and outlook

A primary focus of this work is to characterize the impacts of uncorrelated sensor noise (USN) on eddy covariance (EC) flux measurements and errors. Our analysis employed the NAAMES airborne dataset and examined air-sea VOC fluxes over the North Atlantic; more broadly, the results shed light on EC sampling regimes where flux magnitudes are modest relative to the noise performance of the sensor. Here we built on prior work (Langford et al., 2015) to quantify the systematic and random flux errors that arise from random instrument errors in the form of USN. The random flux errors propagate linearly from USN, while systematic biases also occur when USN obscures the true wind-scalar time lag. We showed that in a noise-limited regime, an ensemble of flux measurements converges to the truth when the time lag is accurately prescribed—for example, from proximate higher-flux periods, or based on higher-flux compounds. The same is not true when time lags are calculated separately based on each individual flux observation, since under noise-limited conditions the average in this case converges to zero rather than to the true flux. We therefore recommend the former approach when it is feasible.

The impact of measurement noise is typically described in terms of a signal-to-noise ratio (SNR), which inherently relates a strength-of-signal to an associated noise level. In concentration space SNR is computed as the ratio between a concentration magnitude and its random error; however, this quantity is not directly relevant to fluxes because the signal of interest is then no longer the concentration magnitude but rather its turbulent fluctuations. Langford et al. (2015) derived a concentration variance SNR as the ratio between turbulence-driven concentration variability and noise driven concentration variability ($\frac{\sigma_{s,turb}^2}{\sigma_{USN}^2}$); this quantity is more flux-relevant but does not by itself fully describe flux detectability. Here we extended the above concepts to define flux SNR as the ratio between a flux and its total random error ($SNR_f = \frac{f}{\sigma_{f,RE}}$). We used noise-perturbation experiments to describe the behavior of SNR_f across a range of noise levels and sampling conditions. The results reveal a transition between i) a noise-limited regime where SNR_f is determined by USN, and ii) a turbulence-limited regime where SNR_f plateaus to a maximum value that is dictated by the stochastic nature of turbulence. For NAAMES, the measured H_2O fluxes fall within the turbulence-limited regime, the sensible heat fluxes fall partly in the turbulence-limited regime and partly in the transitional regime, and the VOC fluxes fall mainly in the noise-limited regime. The overall results provide a framework for determining the sensor noise performance that would

be needed to obtain a desired SNR_f under a given set of sampling conditions. For example, we found that decreasing USN by 7-23× compared to the instrument deployed during NAAMES (Müller et al., 2014) would have increased the fraction of detectable VOC fluxes for the data subset examined here from 17 % to 75 %. The same SNR_f criterion would also minimize the USN-driven systematic errors discussed above. Future work could extend these findings by exploring the extent to which different measurement frequencies may mitigate USN impacts, and the resulting trade-offs with high-frequency flux attenuation.

Given the above context, we interpreted the air-sea VOC exchange rates measured during NAAMES. Fluxes were universally downward for acetone and universally upward for DMS, and in both cases were broadly comparable to prior estimates for the same region. Several compounds (e.g., acetaldehyde, methanol, MEK) showed evidence of bi-directional exchange. In many other cases, USN effects limited the number of individual measurements with $SNR_f > 3$, but the predominantly random nature of those errors allowed us to average the data to obtain a tighter constraint on the campaign-mean flux. Updated VOC sensors with improved USN performance could be used to go beyond results here in deriving needed process insights related to surface-air exchange.

Code availability

Flux analyses presented here are based on a Matlab toolbox publicly available at https://github.com/AirChem/FluxToolbox.

Data availability

NAAMES data are publicly available at http://doi.org/10.5067/SUBORBITAL/NAAMES/DATA001. The high-resolution wind and VOC data employed in this analysis are available at https://z.umn.edu/b0gw and will be archived in a community-recognized public repository at the time of publication.

Author contributions

XC, DBM, and GMW designed the study. AW, MM, and AS provided VOC measurements. KLT provided wind, water vapor, and potential temperature data. XC, DBM, GMW, ERD, and MJD led the analyses. XC and DBM led the manuscript preparation, with contributions from all authors.

Competing interests

One of the co-authors is a member of the editorial board for Atmospheric Measurement Techniques. The authors also have no other competing interests to declare.

Acknowledgements

DBM acknowledges support from the National Aeronautics and Space Administration (NASA grant #80NSSC24K0480). NAAMES was funded by the NASA EVS-2 program. We thank the NAAMES investigation team for making this work possible, and NASA's ASDC DAAC for curating and distributing the NAAMES data. GMW and ERD acknowledge support from the NASA Tropospheric Chemistry Program. High performance computing resources utilized in this work were provided by the Minnesota Supercomputing Institute (https://msi.umn.edu) at the University of Minnesota.

PTR-ToF-MS measurements onboard the NASA C-130 during NAAMES were supported by the Austrian Federal Ministry for Transport, Innovation and Technology (bmvit) through the Austrian Space Applications Programme (ASAP; grant nos. 833451, 840086, and 847967) of the Austrian Research Promotion Agency (FFG) and by the Tiroler Wissenschaftsförderung (TWF; grant no. UNI-0404/1895). Support from the PTR-TOF-MS instrument team (Phillip Eichler, Tomas Mikoviny, Felix Piel) and from IONICON Analytik GmbH is gratefully acknowledged. We thank John Barrick for his help in integrating the TAMMS instrument onto the C-130 and helping with the placement and engineering of the meteorological sensors necessary for the NAAMES mission. We thank Ryan Bennet and Michael Shook for helpful data processing and interpretation. We thank Gordon Novak and Michael Vermuel for insightful discussions. We acknowledge Eric Apel and Rebecca Hornbrook for their work in obtaining the ATom TOGA measurements, and NASA's ORNL DAAC for ATom data maintenance.

References

Apel, E. C., Asher, E. C., Hills, A. J., and Hornbrook, R. S.: ATom: Volatile Organic Compounds (VOCs) from the TOGA instrument, Version 2. NASA's Oak Ridge National Laboratory (ORNL) Distributed Active Archive Center (DAAC). Accessed: 2026-01-21, https://doi.org/10.3334/ORNLDAAC/1936, 2021.

Bandy, A. R., Thornton, D. C., Tu, F. H., Blomquist, B. W., Nadler, W., Mitchell, G. M., and Lenschow, D. H.: Determination of the vertical flux of dimethyl sulfide by eddy correlation and atmospheric pressure ionization mass spectrometry (APIMS), J. Geophys. Res.: Atmos., 107, https://doi.org/10.1029/2002JD002472, 2002.

Banerjee, T., Katul, G. G., Zahn, E., Dias, N. L., and Bou-Zeid, E.: A Single Compartment Relaxed Eddy Accumulation Method, J. Geophys. Res.: Atmos., 129, https://doi.org/10.1029/2024JD040811, 2024.

Bates, K. H., Jacob, D. J., Wang, S. Y., Hornbrook, R. S., Apel, E. C., Kim, M. J., Millet, D. B., Wells, K. C., Chen, X., Brewer, J. F., Ray, E. A., Commane, R., Diskin, G. S., and Wofsy, S. C.: The Global Budget of Atmospheric Methanol: New Constraints on Secondary, Oceanic, and Terrestrial Sources, J. Geophys. Res.: Atmos., 126, https://doi.org/10.1029/2020JD033439, 2021.

Beale, R., Dixon, J. L., Smyth, T. J., and Nightingale, P. D.: Annual study of oxygenated volatile organic compounds in UK shelf waters, Mar. Chem., 171, 96-106, https://doi.org/10.1016/j.marchem.2015.02.013, 2015.

Beale, R., Dixon, J. L., Arnold, S. R., Liss, P. S., and Nightingale, P. D.: Methanol, acetaldehyde, and acetone in the surface waters of the Atlantic Ocean, J. Geophys. Res.: Oceans, 118, 5412-5425, https://doi.org/10.1002/jgrc.20322, 2013.

Behrenfeld, M. J.: Abandoning Sverdrup's Critical Depth Hypothesis on phytoplankton blooms, Ecology, 91, 977-989, https://doi.org/10.1890/09-1207.1, 2010.

Behrenfeld, M. J., and Boss, E. S.: Student's tutorial on bloom hypotheses in the context of phytoplankton annual cycles, Glob. Chang. Biol., 24, 55-77, https://doi.org/10.1111/gcb.13858, 2018.

Behrenfeld, M. J., Moore, R. H., Hostetler, C. A., Graff, J., Gaube, P., Russell, L. M., Chen, G., Doney, S. C., Giovannoni, S., Liu, H., Proctor, C., Bolaños, L. M., Baetge, N., Davie-Martin, C., Westberry, T. K., Bates, T. S., Bell, T. G., Bidle, K. D., Boss, E. S., Brooks, S. D., Cairns, B., Carlson, C., Halsey, K., Harvey, E. L., Hu, C., Karp-Boss, L., Kleb, M., Menden-Deuer, S., Morison, F., Quinn, P. K., Scarino, A. J., Anderson, B., Chowdhary, J., Crosbie, E., Ferrare, R., Haire, J. W., Hu, Y., Janz, S., Redemann, J., Saltzman, E., Shook, M., Siegel, D. A., Wisthaler, A., Martine, M. Y., and Ziemba, L.: The North Atlantic Aerosol and Marine Ecosystem Study (NAAMES): Science Motive and Mission Overview, Front. Mar. Sci., 6, https://doi.org/10.3389/fmars.2019.00122, 2019.

Bell, T. G., Porter, J. G., Wang, W. L., Lawler, M. J., Boss, E., Behrenfeld, M. J., and Saltzman, E. S.: Predictability of Seawater DMS During the North Atlantic Aerosol and Marine Ecosystem Study (NAAMES), Front. Mar. Sci., 7, https://doi.org/10.3389/fmars.2020.596763, 2021.

Brewer, J. F., Fischer, E., Commane, R., Wofsy, S. C., Daube, B. C., Apel, E. C., Hills, A. J., Hornbrook, R. S., Barletta, B., Meinardi, S., Blake, D. R., Ray, E. A., and Ravishankara, A. R.: Evidence for an Oceanic Source of Methyl Ethyl Ketone to the Atmosphere, Geophys. Res. Lett., 47, https://doi.org/10.1029/2019GL086045, 2020.

Carpenter, L. J., Archer, S. D., and Beale, R.: Ocean-atmosphere trace gas exchange, Chem. Soc. Rev., 41, 6473-6506, https://doi.org/10.1039/c2cs35121h, 2012.

Conley, S. A., Faloona, I., Miller, G. H., Lenschow, D. H., Blomquist, B., and Bandy, A.: Closing the dimethyl sulfide budget in the tropical marine boundary layer during the Pacific Atmospheric Sulfur Experiment, Atmos. Chem. Phys., 9, 8745-8756, https://doi.org/10.5194/acp-9-8745-2009, 2009.

Davie-Martin, C. L., Giovannoni, S. J., Behrenfeld, M. J., Penta, W. B., and Halsey, K. H.: Seasonal and Spatial Variability in the Biogenic Production and Consumption of Volatile Organic Compounds (VOCs) by Marine Plankton in the North Atlantic Ocean, Front. Mar. Sci., 7, https://doi.org/10.3389/fmars.2020.611870, 2020.

de Gouw, J. A., Warneke, C., Parrish, D. D., Holloway, J. S., Trainer, M., and Fehsenfeld, F. C.: Emission sources and ocean uptake of acetonitrile (CH3CN) in the atmosphere, J. Geophys. Res.: Atmos., 108, https://doi.org/10.1029/2002jd002897, 2003.

Deventer, M. J., Griffis, T. J., Roman, D. T., Kolka, R. K., Wood, J. D., Erickson, M., Baker, J. M., and Millet, D. B.: Error characterization of methane fluxes and budgets derived from a long-term comparison of open- and

closed-path eddy covariance systems, Agric. For. Meteorol., 278, https://doi.org/10.1016/j.agrformet.2019.107638, 2019.
Donahue, N. M., and Prinn, R. G.: Nonmethane Hydrocarbon Chemistry in the Remote Marine Boundary-Layer, J. Geophys. Res.: Atmos., 95, 18387-18411, https://doi.org/10.1029/JD095iD11p18387, 1990.
Dong, Y., Yang, M., Bakker, D. C. E., Kitidis, V., and Bell, T. G.: Uncertainties in eddy covariance air-sea CO flux measurements and implications for gas transfer velocity parameterisations, Atmos. Chem. Phys., 21, 8089-8110, https://doi.org/10.5194/acp-21-8089-2021, 2021.
Faloona, I., Lenschow, D. H., Campos, T., Stevens, B., van Zanten, M., Blomquist, B., Thornton, D., Bandy, A., and Gerber, H.: Observations of entrainment in eastern Pacific marine stratocumulus using three conserved scalars, J. Atmos. Sci., 62, 3268-3285, https://doi.org/10.1175/JAS3541.1, 2005.
Fischer, E. V., Jacob, D. J., Millet, D. B., Yantosca, R. M., and Mao, J.: The role of the ocean in the global atmospheric budget of acetone, Geophys. Res. Lett., 39, https://doi.org/10.1029/2011gl050086, 2012.
Göckede, M., Kittler, F., and Schaller, C.: Quantifying the impact of emission outbursts and non-stationary flow on eddy-covariance CH4 flux measurements using wavelet techniques, Biogeosciences, 16, 3113-3131, https://doi.org/10.5194/bg-16-3113-2019, 2019.
Hackenberg, S. C., Andrews, S. J., Airs, R., Arnold, S. R., Bouman, H. A., Brewin, R. J. W., Chance, R. J., Cummings, D., Dall'Olmo, G., Lewis, A. C., Minaeian, J. K., Reifel, K. M., Small, A., Tarran, G. A., Tilstone, G. H., and Carpenter, L. J.: Potential controls of isoprene in the surface ocean, Global Biogeochem. Cycles, 31, 644-662, https://doi.org/10.1002/2016GB005531, 2017.
Hintsa, E. J., Dacey, J. W. H., McGillis, W. R., Edson, J. B., Zappa, C. J., and Zemmelink, H. J.: Sea-to-air fluxes from measurements of the atmospheric gradient of dimethylsulfide and comparison with simultaneous relaxed eddy accumulation measurements, J. Geophys. Res.: Oceans, 109, https://doi.org/10.1029/2002JC001617, 2004.
Hoffmann, E. H., Tilgner, A., Schrödner, R., Bräuer, P., Wolke, R., and Herrmann, H.: An advanced modeling study on the impacts and atmospheric implications of multiphase dimethyl sulfide chemistry, Proc. Natl. Acad. Sci. U. S. A., 113, 11776-11781, https://doi.org/10.1073/pnas.1606320113, 2016.
Karl, T., Misztal, P. K., Jonsson, H. H., Shertz, S., Goldstein, A. H., and Guenther, A. B.: Airborne Flux Measurements of BVOCs above Californian Oak Forests: Experimental Investigation of Surface and Entrainment Fluxes, OH Densities, and Damkohler Numbers, J. Atmos. Sci., 70, 3277-3287, https://doi.org/10.1175/JAS-D-13-054.1, 2013.
Kettle, A. J., Rhee, T. S., von Hobe, M., Poulton, A., Aiken, J., and Andreae, M. O.: Assessing the flux of different volatile sulfur gases from the ocean to the atmosphere, J. Geophys. Res.: Atmos., 106, 12193-12209, https://doi.org/10.1029/2000JD900630, 2001.
Kiene, R. P., Williams, T. E., Esson, K., Tortell, P. D., and Dacey, J. W. H.: Methanethiol Concentrations and Sea-Air Fluxes in the Subarctic NE Pacific Ocean, American Geophysical Union, Fall meeting, 2017.
Kim, M. J., Novak, G. A., Zoerb, M. C., Yang, M., Blomquist, B. W., Huebert, B. J., Cappa, C. D., and Bertram, T. H.: Air-Sea exchange of biogenic volatile organic compounds and the impact on aerosol particle size distributions, Geophys. Res. Lett., 44, 3887-3896, https://doi.org/10.1002/2017GL072975, 2017.
Land, P. E., Shutler, J. D., Bell, T. G., and Yang, M.: Exploiting satellite earth observation to quantify current global oceanic DMS flux and its future climate sensitivity, J. Geophys. Res.: Oceans, 119, 7725-7740, https://doi.org/10.1002/2014JC010104, 2014.
Langford, B., Acton, W., Ammann, C., Valach, A., and Nemitz, E.: Eddy-covariance data with low signal-to-noise ratio: time-lag determination, uncertainties and limit of detection, Atmos. Meas. Tech., 8, 4197-4213, https://doi.org/10.5194/amt-8-4197-2015, 2015.
Lawson, S. J., Law, C. S., Harvey, M. J., Bell, T. G., Walker, C. F., de Bruyn, W. J., and Saltzman, E. S.: Methanethiol, dimethyl sulfide and acetone over biologically productive waters in the southwest Pacific Ocean, Atmos. Chem. Phys., 20, 3061-3078, https://doi.org/10.5194/acp-20-3061-2020, 2020.
Lenschow, D. H.: Probing the Atmospheric Boundary Layer, Am. Meteorol. Soc., Boston, Mass., edited by: Lenschow, D. H., 1986.
Lenschow, D. H., and Kristensen, L.: Uncorrelated Noise in Turbulence Measurements, J. Atmos. Ocean. Technol., 2, 68-81, https://doi.org/10.1175/1520-0426(1985)002<0068:UNITM>2.0.CO;2, 1985a.

Lenschow, D. H., and Kristensen, L.: Uncorrelated Noise in Turbulence Measurements. NCAR Tech. Note; NCAR/TN-254+STR, 59 pp. [Available from NCAR, P.O. Box 3000, Boulder, CO 80307.], https://doi.org/10.5065/D6BZ640M, 1985b.

Lenschow, D. H., Mann, J., and Kristensen, L.: How Long Is Long Enough When Measuring Fluxes and Other Turbulence Statistics?, J. Atmos. Ocean. Technol., 11, 661-673, https://doi.org/10.1175/1520-0426(1994)011<0661:HLILEW>2.0.CO;2, 1994.

Lenschow, D. H., Wulfmeyer, V., and Senff, C.: Measuring second- through fourth-order moments in noisy data, J. Atmos. Ocean. Technol., 17, 1330-1347, https://doi.org/10.1175/1520-0426(2000)017<1330:MSTFOM>2.0.CO;2, 2000.

Li, Q., Jacob, D. J., Yantosca, R. M., Heald, C. L., Singh, H. B., Koike, M., Zhao, Y., Sachse, G. W., and Streets, D. G.: A global three-dimensional model analysis of the atmospheric budgets of HCN and CH3CN: Constraints from aircraft and ground measurements, J. Geophys. Res.: Atmos., 108, https://doi.org/10.1029/2002JD003075, 2003.

Liss, P. S., and Slater, P. G.: Flux of Gases across the Air-Sea Interface, Nature, 247, 181-184, https://doi.org/10.1038/247181a0, 1974.

Liu, Y., Liang, X. S., and Weisberg, R. H.: Rectification of the bias in the wavelet power spectrum, J. Atmos. Ocean. Technol., 24, 2093-2102, https://doi.org/10.1175/2007JTECHO511.1, 2007.

Marandino, C. A., De Bruyn, W. J., Miller, S. D., Prather, M. J., and Saltzman, E. S.: Oceanic uptake and the global atmospheric acetone budget, Geophys. Res. Lett., 32, https://doi.org/10.1029/2005gl023285, 2005.

Marandino, C. A., De Bruyn, W. J., Miller, S. D., and Saltzman, E. S.: Eddy correlation measurements of the air/sea flux of dimethylsulfide over the North Pacific Ocean, J. Geophys. Res.: Atmos., 112, https://doi.org/10.1029/2006JD007293, 2007.

Marandino, C. A., De Bruyn, W. J., Miller, S. D., and Saltzman, E. S.: DMS air/sea flux and gas transfer coefficients from the North Atlantic summertime coccolithophore bloom, Geophys. Res. Lett., 35, https://doi.org/10.1029/2008GL036370, 2008.

Marandino, C. A., De Bruyn, W. J., Miller, S. D., and Saltzman, E. S.: Open ocean DMS air/sea fluxes over the eastern South Pacific Ocean, Atmos. Chem. Phys., 9, 345-356, https://doi.org/10.5194/acp-9-345-2009, 2009.

Marandino, C. A., Tegtmeier, S., Krüger, K., Zindler, C., Atlas, E. L., Moore, F., and Bange, H. W.: Dimethylsulphide (DMS) emissions from the western Pacific Ocean: a potential marine source for stratospheric sulphur?, Atmos. Chem. Phys., 13, 8427-8437, https://doi.org/10.5194/acp-13-8427-2013, 2013.

Miller, S., Marandino, C., de Bruyn, W., and Saltzman, E. S.: Air-sea gas exchange of CO2 and DMS in the North Atlantic by eddy covariance, Geophys. Res. Lett., 36, https://doi.org/10.1029/2009GL038907, 2009.

Millet, D. B., Guenther, A., Siegel, D. A., Nelson, N. B., Singh, H. B., de Gouw, J. A., Warneke, C., Williams, J., Eerdekens, G., Sinha, V., Karl, T., Flocke, F., Apel, E., Riemer, D. D., Palmer, P. I., and Barkley, M.: Global atmospheric budget of acetaldehyde: 3-D model analysis and constraints from in-situ and satellite observations, Atmos. Chem. Phys., 10, 3405-3425, https://doi.org/10.5194/acp-10-3405-2010, 2010.

Misztal, P. K., Karl, T., Weber, R., Jonsson, H. H., Guenther, A. B., and Goldstein, A. H.: Airborne flux measurements of biogenic isoprene over California, Atmos. Chem. Phys., 14, 10631-10647, https://doi.org/10.5194/acp-14-10631-2014, 2014.

Mitchell, G. M.: Determination of vertical fluxes of sulfur dioxide and dimethyl sulfide in the remote marine atmosphere by eddy correlation and an airborne isotopic dilution atmospheric pressure ionization mass spectrometer, Ph.D. thesis, Drexel Univ., Philadelphia, Pa., https://doi.org/10.17918/etd-69, 2001.

Moncrieff, J., Clement, R., Finnigan, J., and Meyers, T.: Chapter 2. Averaging, Detrending, and Filtering of Eddy Covariance Time Series, Handbook of micrometeorology: A guide for surface flux measurement and analysis, edited by: Lee, X., Massman, W., and Law, B., Springer Netherlands, Dordrecht, 7-31 pp., 2005.

Müller, M., Anderson, B. E., Beyersdorf, A. J., Crawford, J. H., Diskin, G. S., Eichler, P., Fried, A., Keutsch, F. N., Mikoviny, T., Thornhill, K. L., Walega, J. G., Weinheimer, A. J., Yang, M., Yokelson, R. J., and Wisthaler, A.: In situ measurements and modeling of reactive trace gases in a small biomass burning plume, Atmos. Chem. Phys., 16, 3813-3824, https://doi.org/10.5194/acp-16-3813-2016, 2016.

Müller, M., Mikoviny, T., Feil, S., Haidacher, S., Hanel, G., Hartungen, E., Jordan, A., Märk, L., Mutschlechner, P., Schottkowsky, R., Sulzer, P., Crawford, J. H., and Wisthaler, A.: A compact PTR-ToF-MS instrument for airborne measurements of volatile organic compounds at high spatiotemporal resolution, Atmos. Meas. Tech., 7, 3763-3772, https://doi.org/10.5194/amt-7-3763-2014, 2014.

NASA/LARC/SD/ASDC: NAAMES C-130 Navigational and Meteorological Data. NASA's Atmospheric Science Data Center (ASDC) Distributed Active Archive Center (DAAC) in the Science Directorate located at NASA Langley Research Center. Accessed: 2026-01-21, https://doi.org/10.5067/ASDC/NAAMES_MetNav_AircraftInSitu_Data_1, 2020.

NASA/LARC/SD/ASDC: NAAMES C-130 Aircraft Merge Data Files. NASA's Atmospheric Science Data Center (ASDC) Distributed Active Archive Center (DAAC) in the Science Directorate located at NASA Langley Research Center. Accessed: 2026-01-21, https://doi.org/10.5067/ASDC/NAAMES_Merge_Data_1, 2022.

Neftel, A., Flechard, C., Ammann, C., Conen, F., Emmenegger, L., and Zeyer, K.: Experimental assessment of N2O background fluxes in grassland systems, Tellus B: Chem. Phys. Meteorol., 59, https://doi.org/10.1111/j.1600-0889.2007.00273.x, 2007.

Novak, G. A., and Bertram, T. H.: Reactive VOC Production from Photochemical and Heterogeneous Reactions Occurring at the Air-Ocean Interface, Acc. Chem. Res., 53, 1014-1023, https://doi.org/10.1021/acs.accounts.0c00095, 2020.

Novak, G. A., Fite, C. H., Holmes, C. D., Veres, P. R., Neuman, J. A., Faloona, I., Thornton, J. A., Wolfe, G. M., Vermeuel, M. P., Jernigan, C. M., Peischl, J., Ryerson, T. B., Thompson, C. R., Bourgeois, I., Warneke, C., Gkatzelis, G. I., Coggon, M. M., Sekimoto, K., Bui, T. P., Dean-Day, J., Diskin, G. S., DiGangi, J. P., Nowak, J. B., Moore, R. H., Wiggins, E. B., Winstead, E. L., Robinson, C., Thornhill, K. L., Sanchez, K. J., Hall, S. R., Ullmann, K., Dollner, M., Weinzierl, B., Blake, D. R., and Bertram, T. H.: Rapid cloud removal of dimethyl sulfide oxidation products limits SO2 and cloud condensation nuclei production in the marine atmosphere, Proc. Natl. Acad. Sci. U. S. A., 118, https://doi.org/10.1073/pnas.2110472118, 2021.

Novak, G. A., Kilgour, D. B., Jernigan, C. M., Vermeuel, M. P., and Bertram, T. H.: Oceanic emissions of dimethyl sulfide and methanethiol and their contribution to sulfur dioxide production in the marine atmosphere, Atmos. Chem. Phys., 22, 6309-6325, https://doi.org/10.5194/acp-22-6309-2022, 2022.

Pagonis, D., Sekimoto, K., and de Gouw, J.: A Library of Proton-Transfer Reactions of H3O+ Ions Used for Trace Gas Detection, J. Am. Soc. Mass. Spectrom., 30, 1330-1335, https://doi.org/10.1007/s13361-019-02209-3, 2019.

Peltola, O., Hensen, A., Helfter, C., Marchesini, L. B., Bosveld, F. C., van den Bulk, W. C. M., Elbers, J. A., Haapanala, S., Holst, J., Laurila, T., Lindroth, A., Nemitz, E., Röckmann, T., Vermeulen, A. T., and Mammarella, I.: Evaluating the performance of commonly used gas analysers for methane eddy covariance flux measurements: the InGOS inter-comparison field experiment, Biogeosciences, 11, 3163-3186, https://doi.org/10.5194/bg-11-3163-2014, 2014.

Pfannerstill, E. Y., Arata, C., Zhu, Q., Schulze, B. C., Ward, R., Woods, R., Harkins, C., Schwantes, R. H., Seinfeld, J. H., Bucholtz, A., Cohen, R. C., and Goldstein, A. H.: Temperature-dependent emissions dominate aerosol and ozone formation in Los Angeles, Science, 384, 1324-1329, https://doi.org/10.1126/science.adg8204, 2024.

Phillips, D. P., Hopkins, F. E., Bell, T. G., Liss, P. S., Nightingale, P. D., Reeves, C. E., Wohl, C., and Yang, M.: Air-sea exchange of acetone, acetaldehyde, DMS and isoprene at a UK coastal site, Atmos. Chem. Phys., 21, 10111-10132, https://doi.org/10.5194/acp-21-10111-2021, 2021.

Pound, R. J., Sherwen, T., Helmig, D., Carpenter, L. J., and Evans, M. J.: Influences of oceanic ozone deposition on tropospheric photochemistry, Atmos. Chem. Phys., 20, 4227-4239, https://doi.org/10.5194/acp-20-4227-2020, 2020.

Rannik, Ü., Peltola, O., and Mammarella, I.: Random uncertainties of flux measurements by the eddy covariance technique, Atmos. Meas. Tech., 9, 5163-5181, https://doi.org/10.5194/amt-9-5163-2016, 2016.

Read, K. A., Carpenter, L. J., Arnold, S. R., Beale, R., Nightingale, P. D., Hopkins, J. R., Lewis, A. C., Lee, J. D., Mendes, L., and Pickering, S. J.: Multiannual observations of acetone, methanol, and acetaldehyde in remote tropical atlantic air: implications for atmospheric OVOC budgets and oxidative capacity, Environ. Sci. Technol., 46, 11028-11039, https://doi.org/10.1021/es302082p, 2012.

Rocco, M., Dunne, E., Peltola, M., Barr, N., Williams, J., Colomb, A., Safi, K., Saint-Macary, A., Marriner, A., Deppeler, S., Harnwell, J., Law, C., and Sellegri, K.: Oceanic phytoplankton are a potentially important source of benzenoids to the remote marine atmosphere, Commun. Earth Environ., 2, https://doi.org/10.1038/s43247-021-00253-0, 2021.

Sanchez, K. J., Chen, C.-L., Russell, L. M., Betha, R., Liu, J., Price, D. J., Massoli, P., Ziemba, L. D., Crosbie, E. C., Moore, R. H., Müller, M., Schiller, S. A., Wisthaler, A., Lee, A. K. Y., Quinn, P. K., Bates, T. S., Porter, J., Bell, T. G., Saltzman, E. S., Vaillancourt, R. D., and Behrenfeld, M. J.: Substantial Seasonal Contribution of

Observed Biogenic Sulfate Particles to Cloud Condensation Nuclei, Sci. Rep., 8, 3235, https://doi.org/10.1038/s41598-018-21590-9, 2018.
Schlundt, C., Tegtmeier, S., Lennartz, S. T., Bracher, A., Cheah, W., Krüger, K., Quack, B., and Marandino, C. A.: Oxygenated volatile organic carbon in the western Pacific convective center: ocean cycling, air-sea gas exchange and atmospheric transport, Atmos. Chem. Phys., 17, 10837-10854, https://doi.org/10.5194/acp-17-10837-2017, 2017.
Seinfeld, J. H., and Pandis, S. N.: Atmospheric chemistry and physics: from air pollution to climate change, 2nd edition, Chapter 19, Wiley, 2006.
Singh, H. B., Salas, L., Herlth, D., Kolyer, R., Czech, E., Viezee, W., Li, Q., Jacob, D. J., Blake, D., Sachse, G., Harward, C. N., Fuelberg, H., Kiley, C. M., Zhao, Y., and Kondo, Y.: In situ measurements of HCN and CH3CN over the Pacific Ocean: Sources, sinks, and budgets, J. Geophys. Res.: Atmos., 108, https://doi.org/10.1029/2002jd003006, 2003b.
Singh, H. B., Tabazadeh, A., Evans, M. J., Field, B. D., Jacob, D. J., Sachse, G., Crawford, J. H., Shetter, R., and Brune, W. H.: Oxygenated volatile organic chemicals in the oceans: Inferences and implications based on atmospheric observations and air-sea exchange models, Geophys. Res. Lett., 30, https://doi.org/10.1029/2003gl017933, 2003a.
Sinha, V., Williams, J., Meyerhöfer, M., Riebesell, U., Paulino, A. I., and Larsen, A.: Air-sea fluxes of methanol, acetone, acetaldehyde, isoprene and DMS from a Norwegian fjord following a phytoplankton bloom in a mesocosm experiment, Atmos. Chem. Phys., 7, 739-755, https://doi.org/10.5194/acp-7-739-2007, 2007.
Stevens, B., Lenschow, D. H., Faloona, I., Moeng, C.-H., Lilly, D. K., Blomquist, B., Vali, G., Bandy, A., Campos, T., Gerber, H., Haimov, S., Morley, B., and Thornton, D.: On entrainment rates in nocturnal marine stratocumulus, Q. J. Roy. Meteor. Soc., 129, 3469-3493, https://doi.org/10.1256/qj.02.202, 2003.
Taddei, S., Toscano, P., Gioli, B., Matese, A., Miglietta, F., Vaccari, F. P., Zaldei, A., Custer, T., and Williams, J.: Carbon dioxide and acetone air-sea fluxes over the southern Atlantic, Environ. Sci. Technol., 43, 5218-5222, https://doi.org/10.1021/es8032617, 2009.
Tanimoto, H., Kameyama, S., Iwata, T., Inomata, S., and Omori, Y.: Measurement of air-sea exchange of dimethyl sulfide and acetone by PTR-MS coupled with gradient flux technique, Environ. Sci. Technol., 48, 526-533, https://doi.org/10.1021/es4032562, 2014.
Taylor, J. R.: An Introduction to Error Analysis: The Study of Uncertainties in Physical Measurements, 2nd edition, 1997.
Thompson, C. R., Wofsy, S. C., Prather, M. J., Newman, P. A., Hanisco, T. F., Ryerson, T. B., Fahey, D. W., Apel, E. C., Brock, C. A., Brune, W. H., Froyd, K., Katich, J. M., Nicely, J. M., Peischl, J., Ray, E., Veres, P. R., Wang, S., Allen, H. M., Asher, E., Bian, H., Blake, D., Bourgeois, I., Budney, J., Bui, T. P., Butler, A., Campuzano-Jost, P., Chang, C., Chin, M., Commane, R., Correa, G., Crounse, J. D., Daube, B., Dibb, J. E., DiGangi, J. P., Diskin, G. S., Dollner, M., Elkins, J. W., Fiore, A. M., Flynn, C. M., Guo, H., Hall, S. R., Hannun, R. A., Hills, A., Hintsa, E. J., Hodzic, A., Hornbrook, R. S., Huey, L. G., Jimenez, J. L., Keeling, R. F., Kim, M. J., Kupc, A., Lacey, F., Lait, L. R., Lamarque, J.-F., Liu, J., McKain, K., Meinardi, S., Miller, D. O., Montzka, S. A., Moore, F. L., Morgan, E. J., Murphy, D. M., Murray, L. T., Nault, B. A., Neuman, J. A., Nguyen, L., Gonzalez, Y., Rollins, A., Rosenlof, K., Sargent, M., Schill, G., Schwarz, J. P., St. Clair, J. M., Steenrod, S. D., Stephens, B. B., Strahan, S. E., Strode, S. A., Sweeney, C., Thames, A. B., Ullmann, K., Wagner, N., Weber, R., Weinzierl, B., Wennberg, P. O., Williamson, C. J., Wolfe, G. M., and Zeng, L.: The NASA Atmospheric Tomography (ATom) Mission Imaging the Chemistry of the Global Atmosphere, Bull. Am. Meteorol. Soc., 103, E761-E790, https://doi.org/10.1175/BAMS-D-20-0315.1, 2022.
Thornhill, K. L., Anderson, B. E., Barrick, J. D. W., Bagwell, D. R., Friesen, R., and Lenschow, D. H.: Air motion intercomparison flights during Transport and Chemical Evolution in the Pacific (TRACE-P)/ACE-ASIA, J. Geophys. Res.: Atmos., 108, https://doi.org/10.1029/2002JD003108, 2003.
Torrence, C., and Compo, G. P.: A practical guide to wavelet analysis, Bull. Am. Meteorol. Soc., 79, 61-78, https://doi.org/10.1175/1520-0477(1998)079<0061:APGTWA>2.0.CO;2, 1998.
Uning, R., Latif, M. T., Hamid, H. H. A., Nadzir, M. S. M., Khan, M. F., and Suratman, S.: Sea-to-Air Fluxes of Isoprene and Monoterpenes in the Coastal Upwelling Region of Peninsular Malaysia, ACS Earth Space Chem., 5, 3429-3436, https://doi.org/10.1021/acsearthspacechem.1c00270, 2021.

Vermeuel, M. P., Novak, G. A., Jernigan, C. M., and Bertram, T. H.: Diel Profile of Hydroperoxymethyl Thioformate: Evidence for Surface Deposition and Multiphase Chemistry, Environ. Sci. Technol., 54, 12521-12529, https://doi.org/10.1021/acs.est.0c04323, 2020.

Wang, S., Apel, E. C., Schwantes, R. H., Bates, K. H., Jacob, D. J., Fischer, E., Hornbrook, R. S., Hills, A. J., Emmons, L. K., Pan, L. L., Honomichl, S., Tilmes, S., Lamarque, J.-F., Yang, M., Marandino, C. A., Saltzman, E. S., de Bruyn, W., Kameyama, S., Tanimoto, H., Omori, Y., Hall, S. R., Ullmann, K., Ryerson, T. B., Thompson, C. R., Peischl, J., Daube, B. C., Commane, R., McKain, K., Sweeney, C., Thames, A. B., Miller, D. O., Brune, W. H., Diskin, G. S., DiGangi, J. P., and Wofsy, S. C.: Global Atmospheric Budget of Acetone: Air-Sea Exchange and the Contribution to Hydroxyl Radicals, J. Geophys. Res.: Atmos., 125, https://doi.org/10.1029/2020JD032553, 2020.

Wang, S., Hornbrook, R. S., Hills, A., Emmons, L. K., Tilmes, S., Lamarque, J.-F., Jimenez, J. L., Campuzano-Jost, P., Nault, B. A., Crounse, J. D., Wennberg, P. O., Kim, M., Allen, H., Ryerson, T. B., Thompson, C. R., Peischl, J., Moore, F., Nance, D., Hall, B., Elkins, J., Tanner, D., Huey, L. G., Hall, S. R., Ullmann, K., Orlando, J. J., Tyndall, G. S., Flocke, F. M., Ray, E., Hanisco, T. F., Wolfe, G. M., St. Clair, J., Commane, R., Daube, B., Barletta, B., Blake, D. R., Weinzierl, B., Dollner, M., Conley, A., Vitt, F., Wofsy, S. C., Riemer, D. D., and Apel, E. C.: Atmospheric Acetaldehyde: Importance of Air-Sea Exchange and a Missing Source in the Remote Troposphere, Geophys. Res. Lett., 46, 5601-5613, https://doi.org/10.1029/2019GL082034, 2019.

Warneke, C., and de Gouw, J. A.: Organic trace gas composition of the marine boundary layer over the northwest Indian Ocean in April 2000, Atmos. Environ., 35, 5923-5933, https://doi.org/10.1016/S1352-2310(01)00384-3, 2001.

Williams, J., Holzinger, R., Gros, V., Xu, X., Atlas, E., and Wallace, D. W. R.: Measurements of organic species in air and seawater from the tropical Atlantic, Geophys. Res. Lett., 31, https://doi.org/10.1029/2004gl020012, 2004.

Wofsy, S. C., Afshar, S., Allen, H. M., Apel, E., Asher, E. C., Barletta, B., Bent, J., Bian, H., Biggs, B. C., Blake, D. R., Blake, N., Bourgeois, I., Brock, C. A., Brune, W. H., Budney, J. W., Bui, T. P., Butler, A., Campuzano-Jost, P., Chang, C. S., Chin, M., Commane, R., Correa, G., Crounse, J. D., Cullis, P. D., Daube, B. C., Day, D. A., Dean-Day, J. M., Dibb, J. E., DiGangi, J. P., Diskin, G. S., Dollner, M., Elkins, J. W., Erdesz, F., Fiore, A. M., Flynn, C. M., Froyd, K., Gesler, D. W., Hall, S. R., Hanisco, T. F., Hannun, R. A., Hills, A. J., Hintsa, E. J., Hoffman, A., Hornbrook, R. S., Huey, L. G., Hughes, S., Jimenez, J. L., Johnson, B. J., Katich, J. M., Keeling, R. F., Kim, M. J., Kupc, A., Lait, L. R., McKain, K., Mclaughlin, R. J., Meinardi, S., Miller, D. O., Montzka, S. A., Moore, F. L., Morgan, E. J., Murphy, D. M., Murray, L. T., Nault, B. A., Neuman, J. A., Newman, P. A., Nicely, J. M., Pan, X., Paplawsky, W., Peischl, J., Prather, M. J., Price, D. J., Ray, E. A., Reeves, J. M., Richardson, M., Rollins, A. W., Rosenlof, K. H., Ryerson, T. B., Scheuer, E., Schill, G. P., Schroder, J. C., Schwarz, J. P., St. Clair, J. M., Steenrod, S. D., Stephens, B. B., Strode, S. A., Sweeney, C., Tanner, D., Teng, A. P., Thames, A. B., Thompson, C. R., Ullmann, K., Veres, P. R., Wagner, N. L., Watt, A., Weber, R., Weinzierl, B., Wennberg, P. O., Williamson, C. J., Wilson, J. C., Wolfe, G. M., Woods, C. T., Zeng, L., and Vieznor, N.: ATom: Merged Atmospheric Chemistry, Trace Gases, and Aerosols, Version 2. NASA's Oak Ridge National Laboratory (ORNL) Distributed Active Archive Center (DAAC). Accessed: 2026-01-21, https://doi.org/10.3334/ORNLDAAC/1925, 2021.

Wohl, C., Li, Q., Cuevas, C. A., Fernandez, R. P., Yang, M., Saiz-Lopez, A., and Simó, R.: Marine biogenic emissions of benzene and toluene and their contribution to secondary organic aerosols over the polar oceans, Sci. Adv., 9, eadd9031, https://doi.org/10.1126/sciadv.add9031, 2023.

Wohl, C., Villamayor, J., Galí, M., Mahajan, A. S., Fernández, R. P., Cuevas, C. A., Bossolasco, A., Li, Q., Kettle, A. J., Williams, T., Sarda-Esteve, R., Gros, V., Simó, R., and Saiz-Lopez, A.: Marine emissions of methanethiol increase aerosol cooling in the Southern Ocean, Sci. Adv., 10, eadq2465, https://doi.org/10.1126/sciadv.adq2465, 2024.

Wolfe, G. M., Hanisco, T. F., Arkinson, H. L., Bui, T. P., Crounse, J. D., Dean-Day, J., Goldstein, A., Guenther, A., Hall, S. R., Huey, G., Jacob, D. J., Karl, T., Kim, P. S., Liu, X., Marvin, M. R., Mikoviny, T., Misztal, P. K., Nguyen, T. B., Peischl, J., Pollack, I., Ryerson, T., St. Clair, J. M., Teng, A., Travis, K. R., Ullmann, K., Wennberg, P. O., and Wisthaler, A.: Quantifying sources and sinks of reactive gases in the lower atmosphere using airborne flux observations, Geophys. Res. Lett., 42, 8231-8240, https://doi.org/10.1002/2015GL065839, 2015.

Wolfe, G. M., Kawa, S. R., Hanisco, T. F., Hannun, R. A., Newman, P. A., Swanson, A., Bailey, S., Barrick, J., Thornhill, K. L., Diskin, G., DiGangi, J., Nowak, J. B., Sorenson, C., Bland, G., Yungel, J. K., and Swenson, C. A.: The

NASA Carbon Airborne Flux Experiment (CARAFE): instrumentation and methodology, Atmos. Meas. Tech., 11, 1757-1776, https://doi.org/10.5194/amt-11-1757-2018, 2018.

Yang, M., Beale, R., Liss, P., Johnson, M., Blomquist, B., and Nightingale, P.: Air-sea fluxes of oxygenated volatile organic compounds across the Atlantic Ocean, Atmos. Chem. Phys., 14, 7499-7517, https://doi.org/10.5194/acp-14-7499-2014, 2014b.

Yang, M., Blomquist, B. W., and Nightingale, P. D.: Air-sea exchange of methanol and acetone during HiWinGS: Estimation of air phase, water phase gas transfer velocities, J. Geophys. Res.: Oceans, 119, 7308-7323, https://doi.org/10.1002/2014JC010227, 2014a.

Yang, M., Nightingale, P. D., Beale, R., Liss, P. S., Blomquist, B., and Fairall, C.: Atmospheric deposition of methanol over the Atlantic Ocean, Proc. Natl. Acad. Sci. U. S. A., 110, 20034-20039, https://doi.org/10.1073/pnas.1317840110, 2013.

Yassaa, N., Peeken, I., Zöllner, E., Bluhm, K., Arnold, S., Spracklen, D., and Williams, J.: Evidence for marine production of monoterpenes, Environ. Chem., 5, 391-401, https://doi.org/10.1071/EN08047, 2008.

Yu, H., Guenther, A., Gu, D., Warneke, C., Geron, C., Goldstein, A., Graus, M., Karl, T., Kaser, L., Misztal, P., and Yuan, B.: Airborne measurements of isoprene and monoterpene emissions from southeastern U.S. forests, Sci. Total Environ., 595, 149-158, https://doi.org/10.1016/j.scitotenv.2017.03.262, 2017.

Yuan, B., Kaser, L., Karl, T., Graus, M., Peischl, J., Campos, T. L., Shertz, S., Apel, E. C., Hornbrook, R. S., Hills, A., Gilman, J. B., Lerner, B. M., Warneke, C., Flocke, F. M., Ryerson, T. B., Guenther, A. B., and de Gouw, J. A.: Airborne flux measurements of methane and volatile organic compounds over the Haynesville and Marcellus shale gas production regions, J. Geophys. Res.: Atmos., 120, 6271-6289, https://doi.org/10.1002/2015JD023242, 2015.

Zemmelink, H. J., Gieskes, W. W. C., Klaassen, W., de Groot, H. W., de Baar, H. J. W., Dacey, J. W. H., Hintsa, E. J., and McGillis, W. R.: Simultaneous use of relaxed eddy accumulation and gradient flux techniques for the measurement of sea-to-air exchange of dimethyl sulphide, Atmos. Environ., 36, 5709-5717, https://doi.org/10.1016/S1352-2310(02)00577-0, 2002.

Zheng, G., Wang, Y., Wood, R., Jensen, M. P., Kuang, C., McCoy, I. L., Matthews, A., Mei, F., Tomlinson, J. M., Shilling, J. E., Zawadowicz, M. A., Crosbie, E., Moore, R., Ziemba, L., Andreae, M. O., and Wang, J.: New particle formation in the remote marine boundary layer, Nat. Commun., 12, 527, https://doi.org/10.1038/s41467-020-20773-1, 2021.